

# The Large-scale and Small-scale Clustering of Lyman-Break Galaxies at $2.5 \leq z \leq 5.5$ from the GOODS survey

Kyoungsoo Lee<sup>1,2</sup>, Mauro Giavalisco<sup>2</sup>, Oleg Y. Gnedin<sup>3</sup>, Rachel Somerville<sup>2</sup>, Harry Ferguson<sup>2</sup>, Mark Dickinson<sup>4</sup>, Masami Ouchi<sup>2,5</sup>

## ABSTRACT

We report on the angular correlation function of Lyman-break galaxies (LBGs) at  $z \sim 4$  and  $\sim 5$  from deep samples obtained from the Great Observatories Deep Origins Survey (GOODS). Similar to LBGs at  $z \sim 3$ , the shape of  $w(\theta)$  of the GOODS LBGs is well approximated by a power-law with slope  $\beta \approx 0.6$  at angular separation  $\theta \geq 10$  arcsec. The clustering strength of  $z \sim 4, 5$  LBGs also depends on the rest-frame UV luminosity, with brighter galaxies more strongly clustered than fainter ones, implying a general correlation between halos' mass and LBGs' star-formation rate. At smaller separations,  $w(\theta)$  of deep samples significantly exceeds the extrapolation of the large-scale power-law fit, implying enhanced spatial clustering at scales  $r \leq 1$  Mpc. We also find that bright LBGs statistically have more faint companions on scales  $\theta \lesssim 20$  arcsec than fainter ones, showing that the enhanced small-scale clustering is very likely due to sub-structure, namely the fact that massive halos can host multiple galaxies. A simple model for the halo occupation distribution and the CDM halo mass function reproduce well the observed  $w(\theta)$ . The scaling relationship of the clustering strength with volume density and with redshift is quantitatively consistent with that of CDM halos. A comparison of the clustering strength of three samples of equal luminosity limit at  $z \sim 3, 4$  and  $5$  shows that the LBGs at  $z \sim 5$  are hosted in halos about one order of magnitude less massive than those in the lower redshift bins, suggesting that star-formation was more efficient at higher-redshift.

---

<sup>1</sup>Johns Hopkins University, Baltimore, MD 21218

<sup>2</sup>Space Telescope Science Institute, Baltimore, MD 21218

<sup>3</sup>Ohio State University, Columbus, OH 43210

<sup>4</sup>National Optical Astronomy Observatory, Tucson, AZ 85719

<sup>5</sup>Hubble fellow

*Subject headings:* cosmology: observations — galaxies: distances and redshifts  
— galaxies: evolution — galaxies: formation

## 1. Introduction

In the current theoretical framework of galaxy evolution, the observed spatial clustering of galaxies is interpreted as the clustering of the dark matter halos that host them. Galaxies of different luminosity, spectral type, morphology, etc. are observed to have, in general, different clustering properties, because the specific criteria adopted to select them also select different “types” of halos. For example, since more massive halos have stronger spatial clustering than less massive ones, galaxies selected by criteria that also select the high-end of the halo mass function will be observed to be more clustered than galaxies whose selection criteria correspond to less massive halos. Similarly, the apparent “evolution” of the spatial clustering of galaxies as a function of redshift is interpreted as the result of the specific “mapping” of the selection criteria of the galaxies into a mass range of the halo mass function and of the evolution of the clustering of the halos, which is driven by gravity.

This dependence of galaxy clustering on the selection criteria and how they map into properties of the halos is at the same time bad and good news. It is bad news because it makes it very difficult to use galaxies to infer anything about the evolution of dark matter, and hence on cosmology, unless one knows exactly how to go from galaxies’ properties to halos’ properties, including taking into account the “astrophysical” evolution of the former, a very complex problem. It is good news because, at least for certain type of galaxies and in some simple case, one can expect to learn something about the physical relationship between certain properties of the galaxies and those of the underlying halos, possibly testing some of the key ideas behind our understanding of galaxy evolution.

One important case where the relationship between galaxies and halos is being successfully explored by means of the analysis of the spatial clustering is that of the Lyman–break galaxies. These are star–forming galaxies whose rest–frame UV spectral energy distribution is not severely obscured by dust. This type of sources are very effectively selected by means of their broad–band UV colors, constructed from around the 912 Å Lyman limit, the Ly $\alpha$  forest region (pronounced in broad–band photometry at  $z \gtrsim 2$ ), and the otherwise relatively featureless continuum redward of the Ly $\alpha$  line (e.g. Steidel & Hamilton 1993; Steidel et al. 1995; Madau et al. 1995). The technique is particularly effective at redshifts  $2.5 \lesssim z \lesssim 6$ , where the UV SED is observed at optical wavelengths and hence one can take advantage of the performance of CCD imagers and spectrographs. Large surveys of Lyman–break galaxies have been conducted over the past ten years in this redshift range resulting in large and well

controlled samples, including large spectroscopic ones (e.g. Steidel et al. 2003; Vanzella et al. 2005; Vanzella et al., in preparation), which are well suited for clustering measures.

LBGS have relatively strong spatial clustering with correlation length comparable to that of present-day bright spiral galaxies (Giavalisco et al. 1998; Giavalisco & Dickinson 2001; Porciani & Giavalisco 2002; Adelberger et al. 2005). This has been interpreted as evidence that they are biased tracers of the mass density field (Giavalisco et al. 1998; Adelberger et al. 1998; Giavalisco & Dickinson 2001). This means that these galaxies are preferentially hosted in dark-matter halos with mass at the high-end of the halo mass function (Giavalisco & Dickinson 2001; Foucaud et al. 2003; Adelberger et al. 2005), which have stronger spatial clustering than less massive halos (see, e.g. Mo & White 1996). A key piece of evidence to link the mass of the halo to physical properties of the galaxies came with the discovery that the strength of the spatial clustering of Lyman-break galaxies is a function of their UV luminosity, with brighter galaxies having larger correlation length (Giavalisco & Dickinson 2001; Foucaud et al. 2003; Ouchi et al. 2004; Adelberger et al. 2005). In the halo interpretation, this is explained if brighter galaxies are, on average, hosted in more massive halos. Since the halos mass function is relatively steep, this also implies that the statistical relationship between mass and UV luminosity must be characterized by a correspondingly small scatter (Giavalisco & Dickinson 2001). Because the UV luminosity of Lyman-break galaxies is powered by star formation, this in turns means that the mass and the star-formation rate are relatively tightly correlated or, in other words, that the mass is a primary parameter that controls the star-formation activity of the Lyman-break galaxies.

The next logical step is to try to derive the relationship between mass and star-formation rate, thus testing the basic ideas behind the physical models of star-formation in young galaxies (e.g. White & Rees 1978). Furthermore, the dependence of the clustering strength on the UV luminosity (clustering segregation hereafter) contains direct information on the scaling relationship of the halo clustering strength (bias) with volume density. Since the shape of this relationship depends on the shape of the power spectrum, the observed clustering segregation can be used to test key predictions of the CDM theory (Giavalisco & Dickinson 2001). To do this, however, information on the halo sub-structure, or the halo occupation distribution function (HOD), is also required (e.g. Bullock et al. 2001, Berlind & Weinberg 2002). This function describes the likelihood that one halo contains more than one galaxy and how this depends on its mass. Once the HOD and clustering segregation functions have been measured, then the relationship between mass and UV luminosity (star-formation rate) can be constrained, and a successful model will have to simultaneously reproduce the observed clustering segregation and UV luminosity function.

In principle, the presence of sub-structure and the HOD function can be constrained by

the shape of the angular correlation function and, as we will see later, by the statistics of close pairs of galaxies. In practice, this requires measures with relatively high S/N from large and faint samples, unavailable until recently, since most of the secondary halo–companion galaxies have lower mass than the central galaxy thus less luminous on average. Furthermore, large samples covering a sufficiently wide dynamic range in luminosity are necessary to provide robust measure of the shape of the clustering segregation. Giavalisco & Dickinson (2001) first reported the detection of clustering segregation and measured its shape but with low S/N. Using a deep sample of LBGs at  $z \sim 4$  and 5 obtained with the Subaru telescope and the Suprime camera, Hamana et al. (2004) reported evidence that the angular correlation function of LBGs deviates from a power–law behavior at small angular scales and derived the HOD function to explain the deviation. Using the largest sample of LBGs to date at  $z \sim 3$ , Adelberger et al. (2005) measured the shape of the angular correlation function at large angular separations with high S/N. Their sample, however, is not deep enough to include halo companion galaxies in appreciable number and detect the effect of sub–structures; they could only set an upper limit of 5% to the number of galaxies in common halos.

In this paper we present a study of the clustering properties of Lyman–break galaxies at  $z \sim 4$  and  $\sim 5$  at faint flux levels. We use two deep and relatively large samples obtained with *HST* and ACS during the program of multi–band imaging of the Great Observatories Origins Deep Survey (GOODS). In fact, these ACS samples of  $B_{435}$  and  $V_{606}$ –band dropouts are currently the largest and the most complete at their depth of such galaxies<sup>1</sup>. Since their size is suitable to measure the angular clustering with high S/N, we have embarked on a project to characterize the physical association between the activity of star formation of the galaxies and the properties of the dark matter halos, primarily the mass, thus providing quantitative tests to the CDM hierarchical theory of galaxy formation. Here we present significantly improved measures of clustering segregation down to faint flux ( $z_{350} \sim 27$ ), show direct evidence of sub–structure in the halos and derive the corresponding HOD. We postpone to a following paper the derivation of the relationship between mass and star–formation rate. All magnitudes in this paper are in the AB scale of Gunn & Oke (1975) and, when necessary, we use a world model with  $\Omega_m = 0.3$ ,  $\Omega_\Lambda = 0.7$ ,  $H_0 = 70$ , and baryonic density  $\Omega_b = 0.04$ .

---

<sup>1</sup>Analogous samples have also been obtained during the Hubble Ultra Deep Field survey, which covers a small portion of the GOODS southern field (CDFs) with identical passbands as the primary GOODS survey. While significantly deeper than the GOODS samples, the HUDF ones are much smaller in size because of the minimal areal coverage of the HUDF.

## 2. The Data and The Samples

Deep optical multi-band imaging with *HST* and ACS has been acquired as part of the program of observations of the GOODS. These ACS data consist of a mosaic of images in each of the  $B_{435}$ ,  $V_{606}$ ,  $i_{775}$  and  $z_{850}$  passbands for a total of 3, 2.5, 2.5 and 5 orbits of integration time, respectively, in each of the two GOODS fields. These two fields are centered around the Hubble Deep Field North (HDF-N) and Chandra Deep Field South (CDF-S) and cover approximately  $10' \times 17'$  each, for a total area coverage of about 0.1 square degree. To search for supernovae at high redshift (Riess et al. 2004), the observations in the  $V_{606}$ ,  $i_{775}$  and  $z_{850}$  bands were not done continuously, but sequenced into “epochs” separated by about 45 days from each other. Because the nominal roll of *HST* changes at a rate of about 1 degree per day, this observing strategy resulted in images acquired during different epochs having position angle in the sky differ by integer multiple of 45 degree. This gives the characteristic jagged edges of the GOODS mosaics in the  $V_{606}$ ,  $i_{775}$  and  $z_{850}$  bands. Giavalisco et al. (2004a) present an overall description of the GOODS project, and we refer the reader to that paper for additional details on the ACS observations.

The  $V_{606}$ ,  $i_{775}$  and  $z_{850}$ -band mosaics presented in Giavalisco et al. (2004a,b) only include the first 3 epochs of observations stacked together, while the samples of Lyman-break galaxies at  $z \sim 4$  and  $\sim 5$  that we are about to discuss here have been extracted from the version v1.0 reduction of the ACS data, which include the full stack of the five epochs. The  $B_{435}$ -band mosaic discussed by Giavalisco et al. (2004a), however, already includes all the data, since all the  $B$ -band observations were taken continuously. A complete description of the v1.0 ACS images will be presented in an upcoming paper (Giavalisco et al., in preparation). Detailed information can also be found in the GOODS website, at the link [http://www.stsci.edu/science/goods/v1\\_release\\_readme/h\\_goods\\_v1.0\\_rdm.html](http://www.stsci.edu/science/goods/v1_release_readme/h_goods_v1.0_rdm.html).

We now provide a brief summary of the data reduction and stacking process for the version v1.0 data release. Differently from the version v0.5 public release and from the mosaic discussed in Giavalisco et al. (2004a), for the version v1.0 reduction we have re-processed all the data (including the  $B_{435}$ -band images) using the best calibration and reference files available. We have improved treatments of the geometrical distortions of ACS using updated coefficients together with corrections for the velocity aberration distortion, and we have also improved rejection of cosmic rays and other blemishes. We have stacked the individual exposures together in each band using the drizzling algorithm in two independent phases. In the first phase, images taken in the same filters are sky-subtracted and drizzled onto a common pixel grid at the instrument native scale (0.05 arcsec/pixel). Cosmic rays and deviant pixels are identified during this process and flagged in mask files specifically created for this purpose. Information on detection blemishes (hot pixels, bad columns, etc.) in

post-pipeline masks (which have also been drizzled onto the same grid) is included in the new masks at this time. During the second phase, the images and the mask files are blotted back to the original positions, drizzled again onto a common astrometric grid with scale 0.03 arcsec/pixel, and stacked together. During this process corrections for the ACS geometrical distortion are applied, cosmic rays flagged during the previous processing block are masked out from the stack, and additional, low-level cosmic rays and defects are identified and masked, too. The final stacks reach a  $1-\sigma$  surface brightness limit of 29.00, 29.08, 28.33 and 28.09 mag arcsec<sup>-2</sup> in the  $B_{435}$ ,  $V_{606}$ ,  $i_{775}$  and  $z_{850}$  band, respectively.

We have created the multi-band source catalogs, which is also public and available at the Web site listed above, using the SExtractor package (Bertin & Arnouts 1996). We made the detections using the  $z_{850}$ -band mosaic, and then used a variety of photometric apertures, including isophotal and a suite of circular apertures of varying radius, as "fixed apertures" to carry out matched photometry in all bands. We have measured completeness of the catalogs as a function of size and magnitude of the sources through extensive Monte Carlo simulations, where we have inserted a very large number of model galaxies (169,100) into the ACS mosaic, after convolution with the ACS PSF and after adding the appropriate Poisson and detector noise. We used galaxies with both exponential and  $r^{1/4}$  light profile with random ellipticity and orientation in the sky, as well as unresolved sources, with varying apparent magnitude and size (for the resolved ones), and then retrieved them with identical procedures as for the real galaxies. From these simulations we estimate that the catalogs are  $\approx 50\%$  complete at  $z_{850} \sim 26.5$  for sources with half-light radius  $r_{1/2} \leq 0.2$  arcsec, and about 10% complete at  $z_{850} \sim 27$ . We have also run multi-band simulations for sources with given input spectral energy distribution (SED) to test completeness relative to color selection, as we will discuss in a moment.

We have also used deep ground-based multi-wavelength imaging data to select samples of Lyman-break galaxies at redshifts  $z \sim 3$  ( $U$ -band dropouts) in the CDF-S field, albeit in a larger area than the ACS fields. These data were acquired as part of the program of ancillary observations of the GOODS project. They are described in Giavalisco et al. (2004a), and we refer the reader to that publication for detail. Here we will summarize the key properties of these data. The  $B$  and  $R$  bands were taken with the Wide Field Imager (WFI) at the 2.2m MPG/ESO telescope, while the  $U$ -band observations were carried out with the MOSAIC II Camera at the CTIO 4m telescope. The stacked image in each band covers a contiguous region of approximately 0.4 degree<sup>2</sup>. Some parameters of these data sets are detailed in Table 1.

Samples of star-forming galaxies at  $z \sim 3, 4$  and 5 were photometrically selected using the Lyman Break technique (e.g. Steidel et al. 1999; Madau et al. 1996; Giavalisco et

al. 2004b. ; see also Giavalisco 2002 for a review). The technique and its application to clustering studies (Giavalisco et al. 1998; Adelberger et al. 1998; Giavalisco & Dickinson 2001) have been extensively discussed in the past, and we refer the reader to the cited literature.

Lyman–break galaxies (LBGs) at  $z \sim 4$  and  $\sim 5$ ,  $B_{435}$  and  $V_{606}$ –band dropouts, respectively, were extracted from the GOODS v1.0 r1.1 catalogs using the same color selection criteria described by Giavalisco et al. (2004b), which we report here for convenience. We defined the  $B_{435}$  and  $V_{606}$ –band dropouts as

$$\begin{aligned} (B_{435} - V_{606}) &\leq 1.1 + (V_{606} - z_{850}) \wedge \\ (B_{435} - V_{606}) &\leq 1.1 \wedge V_{606} - z_{850} \geq 1.6, \end{aligned}$$

and

$$\begin{aligned} (V_{606} - i_{775}) &> 1.5 + 0.9 \cdot (i_{775} - z_{850}) \vee \\ (V_{606} - i_{775}) &> 2.0 \wedge (V_{606} - i_{775}) > 1.2 \wedge \\ (i_{775} - z_{850}) &< 1.3, \end{aligned}$$

where the symbols  $\vee$  and  $\wedge$  are the logical "OR" and "AND" operators, respectively. In both cases we have limited the apparent magnitude of the samples to  $z_{850} \leq 27.0$  for completeness. We have also visually inspected each galaxy included in the samples and removed objects with stellar morphology and obvious spurious detections, such as diffraction spikes. Down to adopted flux limit of  $z_{850} \leq 27.0$ , the ACS samples include 2463  $B_{435}$ –band dropouts and 878  $V_{606}$ –band dropouts.

Lyman–break galaxies at  $z \sim 3$  were selected using

$$\begin{aligned} (U - B) &\geq (B - R) + 0.6 \wedge \\ (U - B) &\geq 0.9 \wedge (B - R) \leq 2.5 \end{aligned}$$

This ground–based sample includes 1609 galaxies in the central region of the field which was used for the clustering analysis down to flux limit of  $R \leq 25.5$ . This corresponds to surface densities of  $\Sigma = 1.6, 7.8, 2.8$  galaxies/arcmin<sup>2</sup> for the  $U, B_{435}$  and  $V_{606}$ –dropouts, respectively.

Contamination from galactic stars or lower redshift objects are nearly negligible for the  $B_{435}$  and  $V_{606}$ –band dropouts because they were morphologically culled taking advantage of its high angular resolution. For the ground-based sample for which such culling is not

possible, we impose high signal to noise ratio ( $S/N \geq 10$ ) in order to filter out spurious sources. This also helps relatively homogeneous detection of star-forming galaxies up to a certain magnitude limit when dealing with data such as the GOODS/ACS that has roughly 15 separate pointings with slight overlaps. Even at the cost of losing some fraction of the faintest LBGs, it is desirable for clustering studies to avoid an artificial clustering signature induced by interlopers and inhomogeneity of the data.

### 3. Simulations

At redshift  $z \sim 3$  the selection of Lyman–break galaxies ( $U$ –band dropouts) has been characterized in great detail thanks to the systematic spectroscopic identification of thousands of candidates (e.g. Steidel et al. 2003). In particular, this extensive body of work has shown that the Lyman–break technique is very efficient, with a relatively low rate of contamination from low–redshift interlopers, and has yielded the redshift distribution function  $N(z)$  associated to a given set of color selection criteria. While spectroscopic identifications have been made of Lyman–break galaxies at  $z \sim 4$  and  $\sim 5$  (Steidel et al. 1999), including a number presented in this work (see later), the spectroscopic samples still remain too small for accurate measures of the redshift distribution function associated to a specific color selection. Fortunately, as the  $z \sim 3$  case has demonstrated (Steidel et al. 1999), Monte Carlo simulations are very effective to provide robust estimates of  $N(z)$ , which we need here to derive the spatial clustering from the angular one and to measure the galaxies’ volume density.

The use of simulations consists in creating artificial LBGs over a large redshift range (we used  $2 \leq z \leq 8$ ) with assumed distribution functions of UV luminosity, SED, morphology and size, inserting them in the real images with random orientations and inclinations, detecting them and measuring their “observed” photometry and morphology as if they were real galaxies. We have adjusted the input distribution functions of UV luminosity (UV luminosity function), size and SED so that the observed distribution functions of apparent magnitude, UV colors and size of the simulated galaxies best reproduce the same quantities of the real galaxies. Specifically, we used galaxies with exponential and  $r^{1/4}$  light profile in equal proportions and size extracted from a log–normal distribution function, as described by Ferguson et al. (2004). This method has been first used by Giavalisco et al. (2004b) and Ferguson et al. (2004); its application to the measure of the UV luminosity function of LBGs will be discussed in an upcoming paper (Giavalisco et al., in preparation).

The average redshifts obtained from the simulations are  $z = 3.2 \pm 0.3$ ,  $3.8 \pm 0.3$ ,  $4.9 \pm 0.3$  for  $U$ ,  $B_{435}$  and  $V_{606}$ –band dropouts, respectively. Figure 1 shows the redshift distribution



of simulated LBGs together with that of a subset of LBGs with spectroscopic redshifts.

#### 4. Measuring the clustering properties of Lyman–break Galaxies

We now discuss the measure of angular and spatial clustering of LBGs and other clustering properties that we have carried out from our samples. The primary measure is that of the angular correlation function  $w(\theta)$ , which we deproject with the Limber transform using the redshift distribution function estimated from the simulations (but see later for a discussion on our spectroscopic observations) to derive the spatial correlation length, in the power–law approximation. In our faint samples, the angular correlation function is very well approximated by a power law at large angular separations, roughly  $\theta > 10$  arcsec, but it exceeds the extrapolation of the large–scale power–law fit at small scales. To understand the nature of this excess clustering, which is not observed in bright samples, either our own  $U$ –band dropout sample or even larger ones (e.g. Adelberger et al. 2005), we have carried out an analysis of the mean number of close neighbors around both bright and faint galaxies. We have used the halo occupation distribution (HOD) formalism to predict the shape of  $w(\theta)$  and compare it with our measure.

##### 4.1. The angular correlation function

The inversion of the angular correlation function is a robust method to derive the spatial correlation length if the redshift distribution function is well known (see Giavalisco et al. 1998; Giavalisco & Dickinson 2001; Adelberger et al. 2005). The measure of  $w(\theta)$  is relatively straightforward; however some care is required in the analysis of the random errors, and, above all, of systematic errors, since they can significantly bias the result. Given the relatively small area covered by the GOODS fields and the way the observations have been obtained, the two most significant sources of systematic errors are cosmic variance (the integral constrained bias) and sensitivity fluctuation in the survey, which can mimic a spurious clustering signal.

We have estimated the angular correlation function using the estimator proposed by Landy and Szalay (1993):

$$w_{obs}(\theta) = \frac{DD(\theta) - 2DR(\theta) + RR(\theta)}{RR(\theta)}, \quad (1)$$

where  $DD(\theta)$  is the number of pairs of observed galaxies with angular separations in the range  $(\theta - \delta\theta/2, \theta + \delta\theta/2)$ ,  $RR(\theta)$  is the analogous quantity for random catalogs with the

same geometry as the observed catalog and  $DR(\theta)$  is the number of random galaxy cross pairs. We have used logarithmic binning of the angular separations to obtain a more uniform sampling over the whole range of angular scales that we have probed ( $1 < \theta < 300$  arcsec).

To account for the random errors, we have estimated the error bars for each angular bin by bootstrap resampling of the data (e.g. Benoist et al. 1996, Ling, Barrow & Frenk 1986). We have computed values of  $w(\theta)$  from 100 randomly selected subsets of galaxies and then used the standard deviation of  $w(\theta)$  as our primary error estimate. This method, however, only accounts for random errors appropriate to our samples size, and does not include the uncertainty due to finite size of our samples, because we use the observed galaxies for the error estimate. In other words, the bootstrap method fails to account for fluctuations on scales larger than our survey. We have used Monte Carlo simulations to estimate these fluctuations of  $w(\theta)$  due to cosmic variance and validate our accounting of random errors. We have created a large number of realizations (50) of GOODS samples at  $z \sim 4$  and  $\sim 5$  extracted from a population with the same large-scale clustering properties (i.e. surface density and angular correlation function— see Porciani & Giavalisco 2002 for a description of the method) as the observed galaxies. Since this test aims at estimating the uncertainty induced in the observed  $w(\theta)$  by the large-scale fluctuations of the density field of the parent population of galaxies from which are samples are extracted from, neglecting the small-scale clustering is inconsequential. Each realization simulates an area of the sky of  $1 \text{ degree}^2$  within which we have selected the “GOODS” samples of LBGs. We have measured  $w(\theta)$  in each sample, and derived the standard deviation of the 50 measures at each angular bins and used it as an estimate of the error bar, finding consistent results with the bootstrap method.

To test the dependence of the angular clustering on the luminosity of the galaxies, we have measured the correlation function for various magnitude cuts in both samples. For the  $B_{435}$  and  $V_{606}$ -band dropout samples we have defined sub-samples at  $z_{850} \leq 27.0, 26.5$  and  $26.0$ ; for the  $U$ -band dropouts we have used  $R \leq 25.5, 24.5$  and  $24.0$ . In what follows, we will denote each sub-sample as B(V)270, 265, 260 and U255, 245, 240, respectively.

## 4.2. Correction for sensitivity variations

A possible source of systematic error in surveys such as GOODS, which consist of either mosaics of images (the ACS images) or images taken with CCD mosaics (the ground-based images), is fluctuations of sensitivity across the surveyed area. Such fluctuations, which typically occurs on scales that are a fraction of the linear size of the survey, can be sufficiently strong to mimic the presence of clustering and bias the measures of  $w(\theta)$ .

To estimate this effect in LBGs samples is not straightforward, because these are color-selected as well as flux-limited, and thus the final selection function is a nontrivial function of sensitivity variations in all the different passbands used in the color selection as well as of their respective limiting magnitudes. The best way to take all of these factors into account is to use Monte Carlo simulations. We have generated over 100,000 artificial  $U$  and  $B_{435}$ -band dropouts and placed them at random positions in each of the  $U$ ,  $B$ ,  $R$  and  $B_{435}$ ,  $V_{606}$ ,  $i_{775}$ ,  $z_{850}$  images of the ground-based and ACS survey, respectively (see above for a description of the simulation technique). We have subsequently “detected” the artificial galaxies and subjected them to the same color selection as if they were real  $U$  or  $B_{435}$ -band dropouts. To the extent that this process is a faithful representation of the overall selection function of the survey, the spatial distribution of these color-selected mock galaxies will reflect various systematics including the sensitivity variations across the field, the effects of holes due to saturated sources or large seeing (of our ground-based mosaics) to the applied color-selection and so forth.

The correction factor can be estimated by measuring the angular correlation function,  $w_{sim}(\theta)$ , against a purely random distribution with the same geometry (this should be essentially zero for perfectly homogeneous data). Since  $w(\theta)$  is the excess probability of finding a pair, our previous measurement can be corrected as

$$1 + w_{corr}(\theta) = \frac{1 + w_{raw}(\theta)}{1 + w_{sim}(\theta)} \quad (2)$$

where  $w_{raw}$  is the measurement using the LS estimator,  $w_{sim}$  is the correlation function of artificial galaxies and  $w_{corr}$  is the corrected angular correlation function of the dropouts. While the correction is non-negligible at small scales for the  $U$ -dropouts, it has negligible effect on the ACS data, hence the correction is applied only to the  $U$ -dropout measurement. The subscript of  $w_{corr}(\theta)$  will be dropped hereafter unless stated otherwise.

### 4.3. Integral Constraint

Due to the finite size of any given survey, the correlation function measured from a sample is underestimated by a constant known as the integral constraint, referred to as  $IC$  hereafter:

$$\omega_{true}(\theta) = \omega_{obs}(\theta) + IC \quad (3)$$

Since the  $IC$  underestimates the measure of all scales equally, this also leads to an

overestimate of the correlation slope,  $\beta$ . This can be estimated by doubly integrating  $\omega_{true}$  over the survey area (Roche & Earles 1999).

$$\begin{aligned}
 IC &= \frac{1}{\Omega^2} \int_1 \int_2 \omega_{true}(\theta) d\Omega_1 \Omega_2 \\
 &= \frac{\sum_i RR(\theta_i) \omega_{true}(\theta_i)}{\sum_i RR(\theta_i)} = \frac{\sum_i RR(\theta_i) A_w \theta_i^{-\beta}}{\sum_i RR(\theta_i)} \quad (4)
 \end{aligned}$$

Note that the integral constraint depends on both the size of given survey ( $\Omega$ ) and the galaxy power spectrum (approximated to a power-law ;  $A_w$  and  $\beta$ ). However, once the correlation slope  $\beta$  is fixed,  $IC/A_w$  only depends on the size and the shape of the survey area. Therefore, one needs to make robust estimate of  $\beta$  from the observational data then for a fixed  $\beta$ ,  $IC/A_w$  can be estimated. We calculate the  $IC$ s from random catalogs generated over a field with the same size and the geometry as our survey area with a range of  $A_w$  and  $\beta$ . For each set ( $A_w, \beta$ ) we calculate  $IC$  value using Equation (4) then compute  $\chi^2$  of the measured  $w_{obs}(\theta)$ . Once  $\beta$  and  $IC/A_w$  are robustly measured from the full sample, for other flux-limited samples,  $A_w$  is the only parameter that needs to be fitted as  $w_{model} = A_w(\theta^{-\beta} - (IC/A_w)_0)$  provided that  $\beta$  does not change significantly with samples of different flux-limits. This helps to make reliable measures of the amplitude  $A_w$  for sub-samples that have lower signal-to-noise than the full sample.

For the B270 sample, we find that a set ( $A_w, \beta, IC$ ) = (0.38, 0.6, 0.012) best describes the measures, however, it should be noted that there is degeneracy between  $A_w$  and  $\beta$ . In other words, there is a range of acceptable  $A_w$ s and  $\beta$ s for a fixed  $IC$  value even for high S/N data, hence one needs to somewhat arbitrarily fix the slope within the given range. We fix  $\beta = 0.6$  and  $IC/A_w = 0.039$  for all samples. Similarly, for the  $U$ -band dropouts, we find ( $A_w, \beta, IC$ ) = (0.50, 0.6, 0.012) thus  $IC/A_w = 0.024$ . Note that  $IC/A_w$  is much smaller for the  $U$ -band dropouts due to larger field size, on the other hand, the  $IC$  values for the full sample of the  $B_{435}$  and  $U$ -band dropouts are comparable, because the faint ACS  $B_{435}$  and  $V_{606}$  dropout samples are less clustered (i.e. smaller  $A_w$ ) than the brighter ground-based sample. Using this method, we find  $IC = 0.020$  and  $0.027$  for the B265 and B260 sample and  $IC = 0.024, 0.031$  and  $0.043$  for the V270, V265 and V260 sample, respectively.

When the slope is allowed to vary, the procedure becomes iterative because the derived  $IC$  depends on  $w(\theta)$  and vice versa, and one cannot conveniently set  $IC/A_w$  to be a constant for the fitting. As Adelberger et al. (2005) pointed out, this is often very unstable regardless of the initial guess. Therefore, as a consistency check we estimated the  $IC$  using different method suggested by Adelberger et al. (2005). Their method takes advantage of the fact

that matter fluctuations,  $\sigma_{CDM}^2$  within given survey volume is in the linear regime and can be estimated from the power spectrum with appropriate window function that accounts for the geometry of the survey volume (see their Equation 20). By definition,  $IC$ , the variance of density fluctuation of galaxies is  $IC \approx b^2 \sigma_{CDM}^2$ . We estimate the galaxy bias,  $b$ , from the correlation function itself by using the relation  $b = \sigma_{8,g}/\sigma_8(z)$ , where  $\sigma_{8,g}$  is the galaxy variance in spheres of comoving radius  $8 h^{-1}$  Mpc (Peebles 1980, Equation [59.3]):

$$\sigma_{8,g}^2 = \frac{72(r_0/8h^{-1}Mpc)^\gamma}{(3-\gamma)(4-\gamma)(6-\gamma)2^\gamma} \quad (5)$$

where  $r_0$  is the correlation length inferred from the angular correlation function (see next subsection),  $\gamma = \beta + 1$  and  $\sigma_8(z)$  is the linear matter fluctuation on the same scale extrapolated from  $\sigma_8(0) = 0.9$

When using this method, we find both  $IC$  and  $\beta$  consistent with the previous method, but the  $IC$  values are slightly smaller in most cases. For instance, for the B270 sample, we find  $IC = 0.010$  instead of 0.012, for B265 0.018 instead of 0.020 and so forth, which makes little difference in the fitted  $A_w$  or  $\beta$  values. This may imply that the generic correlation function slope  $\beta$  may be slightly steeper than the fiducial value 0.6 for some sub-samples as can be seen in Table 3. For a fixed  $r_0$ ,  $\sigma_{8,g}$  declines with the slope  $\gamma$  at  $1.5 < \gamma < 2.0$ . However, for a fixed  $\gamma$  (or  $\beta$ ), both methods are in good agreement.

Since the  $IC$  is  $w(\theta)$ -dependent, power-law fitting and correcting for the  $IC$  are in fact simultaneous processes. In each iteration, only the  $w_{obs}(\theta)$  measurement with  $\theta > 10$  arcsec is used for power-law fit (to probe large scale structure) because at  $\theta < 10$  arcsec there may be significant contribution from highly nonlinear small-scale clustering. Figure 2 shows  $w_{obs}(\theta)$  measure for the full  $B_{435}$ -band dropout sample together with the best power-law fit. Clearly, a departure from a pure power-law is apparent on small scales ( $\theta < 10$  arcsec).

Fitting the data to a straight line in logarithmic space helps estimate a more reasonable correlation slope in our case as opposed to fitting to a power-law in linear space because logarithmic binning essentially gives more weight on small scales which are in general noisier due to a small number of galaxy pairs. Therefore, even a slight boost in  $w(\theta)$  can throw off the slope to a much larger value. We also fitted the data using Levenberg–Marquardt nonlinear least squares (Press et al. 1992) in linear angular space, which showed consistently steeper slopes as we expected. For this reason, we adopt the parameters obtained from the linear fit as our best values. To estimate  $1\sigma$  confidence intervals of the parameters  $A_w$  and  $\beta$ , we carried out a large ensemble of random realizations of the measured  $w(\theta)$  assuming normal errors, and calculated best-fit parameter values for each of these synthetic data sets. The fitted values of  $A_w$  and  $\beta$  are specified in Table 3.

#### 4.4. The Spatial Correlation Function $\xi(r)$

We derive the spatial correlation function  $\xi(r)$  by inverting  $w(\theta)$  using the Limber transform (Peebles 1980). If the spatial function has the form  $\xi(r) = (r/r_0)^{-\gamma}$ , the angular correlation function also has to be a power-law,  $w(\theta) = A_w \theta^{-\beta}$  where  $\beta = \gamma - 1$  and  $A_w$  is related to  $\xi(r)$  as,

$$A_w = Cr_0^\gamma \int F(z) D_\theta^{1-\gamma}(z) N(z)^2 g(z) dz \times \left[ \int N(z) dz \right]^{-2}$$

where  $D_\theta$  is the angular diameter distance and  $N(z)$  is the redshift selection function derived from the simulations.

$$g(z) = \frac{H_0}{c} ((1+z)^2 1 + \Omega_0 z + \Omega_\Lambda [(1+z)^{-2} - 1]^{1/2})$$

$$C = \sqrt{\pi} \frac{\Gamma[(\gamma-1)/2]}{\Gamma(\gamma/2)}.$$

The correlation lengths  $r_0$  derived using this method are listed in Table 3. Two different  $r_0$  values derived from the fits with and without the correlation slope  $\beta$  fixed to a fiducial value 0.60, are consistent with each other within the errors. In the following discussion, we regard the former as our best  $r_0$  values.

Best-fit  $r_0$  values range from 2.8  $h^{-1}$  Mpc to 7  $h^{-1}$  Mpc (comoving) depending on the median luminosity of the sub-samples. In each redshift range, brighter samples have larger correlation lengths. We have compared our measures with those from other groups for samples with similar median luminosity and in the same redshift range generally finding good agreement. At  $z \sim 3$  Adelberger et al. (2005) found  $r_0 = 4.0 \pm 0.6 h^{-1}$  Mpc for galaxies with magnitude  $23.5 < \mathcal{R} < 25.5$  ( $\bar{z} = 2.9$ ), in good agreement with our  $R < 25.5$  sample for which we found  $r_0 = 4.0_{-0.2}^{+0.2} h^{-1}$  Mpc. At  $z \sim 4$  and 5, Ouchi et al. (2004) reported  $r_0 = 4.1_{-0.2}^{+0.2}$  and  $5.9_{-1.7}^{+1.3} h^{-1}$  Mpc for their LBGz4s ( $i' \lesssim 26$ ) and LBGz5s ( $z' < 25.8$  for LBGz5s) sample, respectively. Using a template spectrum of LBG that reproduces the median UV colors of the samples, we computed that the flux limit of Ouchi et al. (2004) correspond to  $z_{850} \lesssim 26.0$  and 25.8, for which we find  $r_0 = 5.1_{-0.5}^{+0.4}$  and  $5.30_{-1.0}^{+1.1} h^{-1}$  Mpc. While the correlation lengths of the two samples of  $V_{606}$ -band dropouts are in good agreement, we noticed that Ouchi et al. reported a lower value than ours for the  $B_{435}$ -band dropout sample, although the two measures overlap at the  $\approx 1.3\sigma$  level.

## 5. Results

### 5.1. Dependence of Clustering strength on Luminosity

A number of authors (Giavalisco & Dickinson 2002; Foucaud et al. 2003; Adelberger et al. 2005) have reported the existence of clustering segregation with the UV luminosity for the LBGs, namely of the fact that the galaxies with higher UV luminosity have stronger spatial clustering (e.g. larger spatial correlation length) than fainter ones. We have examined the dependence of the clustering strength of our samples on luminosity using several apparent magnitude cuts constructed from the full samples. Apparent magnitude cuts roughly correspond to absolute magnitude cuts because the luminosity–distance changes only by  $\approx 20\%$  over the redshift range covered by each of our samples, since their redshift selection functions are relatively narrow. Whether or not we fix the correlation slope to a fiducial value of  $\beta = 0.6$  (Porciani & Giavalisco 2002), we find that the correlation amplitude  $A_w$ , and  $r_0$  accordingly, increases with median luminosity.

The correlation length of the  $B_{435}$ –band dropouts increases from  $2.8_{-0.2}^{+0.2} h^{-1}$  to  $3.7_{-0.3}^{+0.3} h^{-1}$  to  $5.1_{-0.5}^{+0.4} h^{-1}$  Mpc with increasing luminosity of the samples (see Tables 3).

Note that the faintest sample of  $B_{435}$ –band dropouts, which is our faintest sample at any redshift, reaching absolute magnitude  $M_{1700} = -18.52$  also has the smallest correlation length,  $r_0 = 2.8 h^{-1}$  Mpc. A similar trend is also found for the  $V_{606}$ –band dropouts. For a fixed absolute luminosity, objects will be fainter at  $z \sim 5$  than its counterpart at  $z \sim 4$  by  $0.6 - 0.7$  mag in  $z_{850}$ –band due to cosmological dimming. This suggests that the correlation lengths for the  $B_{435}$  and  $V_{606}$ –band dropouts for a fixed absolute UV luminosity are comparable (see Table 3 for details).

In agreement with previous results, we find that the  $U$ –band dropouts follow a similar trend, too. For the U255 sample ( $R < 25.5$ ) we measure a correlation length  $r_0 = 4.0_{-0.2}^{+0.2} h^{-1}$  Mpc, in an excellent agreement with the value reported by Adelberger et al. (2005),  $4.0 h^{-1}$  Mpc for roughly the same magnitude threshold ( $\langle R - \mathcal{R} \rangle \sim 0.03$  at  $z \sim 3$  using our mean LBG spectrum). The correlation length increases up to  $r_0 = 7.8_{-0.6}^{+0.5} h^{-1}$  for  $R < 24.0$ . Interestingly, this is comparable to  $8 h^{-1}$  Mpc, the correlation length of a sample of distant–red galaxies (DRGs) found at similar redshifts (Daddi et al. 2003).

The left three panels of Figure 3 show  $w(\theta)$  for the full sample and the brightest subsamples for each dropout flavor together with best–fit power–laws. The power–fits (solid lines) when  $\beta$  is fixed to 0.6 are shown for clarity. The right panels show the derived correlation lengths for these samples. The trend is clear in all samples that brighter samples are more strongly clustered in space.

The sub-samples that we have used to measure clustering segregation are not independent from one another, because the galaxies that compound the brighter samples also belong to the faintest one thus diluting the weak clustering signal from the faintest galaxies. We have repeated the measures using two mutually independent samples that we built by splitting the full  $B_{435}$ -band dropouts sample into two independent magnitude bins,  $26.3 < z_{850} < 27.0$  and  $z_{850} < 26.3$  with roughly equal number of galaxies in each bin. For these two samples we have measured  $r_0 = 4.0^{+0.3}_{-0.3}$  and  $2.3^{+0.5}_{-0.4} h^{-1}$  Mpc, respectively. Note that the correlation length of the faint sample is now smaller than  $2.8^{+0.2}_{-0.2} h^{-1}$  Mpc of the  $z_{850} < 27.0$  sample, consistent with the luminosity segregation.

Recently, Norberg et al. (2001) and Zehavi et al. (2002) observed the luminosity segregation in the optically selected galaxies in local universe with high S/N. They also found that the increase in  $r_0$  becomes more rapid for samples that are brighter than  $L_*$ . Though the scatter between star-formation rate seen in UV and optical wavelengths is unclear thus making direct comparisons of our result to theirs difficult, the results from our brightest  $U$ -band dropouts (for which  $r_0 \sim 8h^{-1}$  Mpc) seem to suggest that we may observe a similar phenomenon at high-redshift, at least,  $z \sim 3$ . Unfortunately, our brightest magnitude cut made to the ACS sample is  $z_{850} = 26.0$ , which is still more than 1 mag fainter than  $m_*$  ( $m_*$  is  $z_{850} \sim 24.7$  and  $24.8$  at  $z = 4$  and  $5$ ) due to a small number of bright sources in the GOODS fields. We plan to extend our observation of luminosity-segregation to higher-luminosity regime at the same redshift intervals ( $z \sim 3 - 5$ ) using a data set that covers much larger area, which will be postponed to a follow-up paper (Lee et al., in preparation).

## 5.2. Small-scale statistics

Our deep ACS data also allow us to probe the existence of sub-structure in the halos that host the most massive LBGs. A general feature of hierarchical clustering is that more massive halos have higher probability than smaller ones to host more than one galaxy (e.g. Berlind & Weinberg 2002). If the existence of clustering segregation is due to the fact that LBGs with higher UV luminosity are, on average, more massive than fainter ones, then one prediction is that brighter LBGs should also show a tendency to have more closely associated galaxies than fainter ones. Our deep ACS sample seems well suited to carry out this test, because satellite galaxies are typically less massive than the central galaxy of the halo (Berlind & Weinberg 2002), and because less massive galaxies apparently have fainter UV luminosity. It is likely that pairs, or multiplets, in which one or more members are significantly fainter than the brightest one are under-represented in the shallower ground-based samples. Unfortunately, the lack of systematic redshift measures prevents us from



identifying individual physical pairs. Our measure will have to be statistical in character, and signal-to-noise will be lost in the projection effect.

In our samples pair statistics on small scales reflect not only large-scale structure of dark matter (via projected close-pairs) but also the physics of galaxy formation within given halos (via physical close-pairs). In this section, we discuss small scale statistics of the ACS selected samples only ( $B_{435}$  and  $V_{606}$ -band dropouts).

As shown in Figure 2, a significant departure from a power-law on small scales is observed in our  $w(\theta)$  measures, most pronounced at  $\theta < 10$  arcsec. This corresponds to roughly  $0.3 - 0.4 h^{-1}$  Mpc comoving at redshift 3 – 5. Recently, Ouchi et al. (2005b) detected a similar small-scale excess in their  $w(\theta)$  measurement of  $z \sim 4$  galaxies selected from a deep wide-field survey in SXDF field (Ouchi et al. 2004). Steepening on small scales seems to be present in all samples, which we verify by fitting the  $w(\theta)$  measurement of each sample to a power-law when the data points with separations  $\theta \leq 10$  arcsec are included, in which case we find that the slope is substantially steeper. The slopes of the power-law fits in both cases are shown in Figure 4 for the  $B_{435}$  and  $V_{606}$ -band dropouts.

This is consistent with the fact that there are two separate contributions to  $w(\theta)$  or  $\xi(r)$ , namely one-halo term and two-halo term, the origins of which are fundamentally different in nature. Two-halo term reflects the spatial distribution of host dark halos by counting galaxy pairs that belong to two distinct halos. This term dominates large-scale behavior of the correlation function and breaks down on small scales due to the halo exclusion effect. In comparison, the one-halo term accounts for galaxy pairs sharing the same halo and is dominant on small scales. This reflects how galaxies populate within given halos. In this context, the single power-law nature of the correlation function seen in the local universe is somewhat coincidental because it requires smooth transition between these two terms to result in pure power-law which is possible only for a certain distribution of galaxies therein. Berlind & Weinberg (2002) argued that the contribution of galaxy pairs in massive galaxy clusters is critical for a smooth transition between these two terms. Clusters must be rare at high redshift, hence this steepening should be more prominent.

Although typical halos at high- $z$  must be much less massive than their present-day counterparts (therefore harboring fewer galaxies per halo), halos at high-mass end may host multiple galaxies. This is consistent with the recent discoveries that protoclusters were already forming by redshift of 4 – 6 (e.g. Ouchi et al. 2005a; Miley et al. 2004). To test for this possibility, we have looked for close galaxy pairs that may share host halos. In light of the luminosity segregation, we have split the full sample based on the  $z_{850}$ -band magnitude because statistically selecting bright galaxies is equivalent to selecting the sites of the most massive dark halos. Since the spectroscopic information is not available, we count galaxy

neighbors around the brightest LBGs as a function of angular separation only.

We split the galaxies in the full ACS sample ( $z \sim 4$ ) into three sub-groups,  $z_{850} \leq 24.0$ ,  $24.0 \leq z_{850} \leq m^*$  and  $25.2 \leq z_{850} \leq 27.0$  where  $m^*$  for the  $B_{435}$ -band dropouts is roughly 24.7. We make a simple assumption that galaxies brighter than  $m^*$  are central galaxies in halos, whereas fainter ones could be satellite galaxies. We count the number of faint neighbors ( $z_{850} > 25.2$ ) around the first two bright groups as a function of angular separation. The upper left panel of Figure 5 shows the average number of neighbors (cumulative counts) around these two bright groups up to 50 arcsec with  $1\sigma$  Poisson error, however, this error should be considered strictly as a lower limit because these are clustered. What is expected for an uncorrelated population with the same surface density is also shown with the dashed line. Due to the clustering, both  $z_{850} \leq 24.0$  and  $24.0 \leq z_{850} \leq m^*$  are well above the dashed line, however,  $z_{850} \leq 24.0$  have more neighbors than the other ( $\approx 2.5\sigma$ ). This cannot be understood in terms of the difference in their clustering strength because the same galaxies (therefore the same clustering strength) are used to be counted as faint neighbors. In addition, there is clearly no reason to believe that bright galaxies have more galaxies along the line of sight which would be included as projected close-pairs. Another way to confirm that the difference does not come from clustering is to look at the same pair counts on larger scales. Upper right panel shows the counts at 100 – 160 arcsec where the two slowly converge. This is because on large scales the contribution from halo-halo clustering dominates the counts thus reflecting the overall clustering strength. To remove the effect coming from the clustering, we take the ratio of the two which is shown in the lower panels of the Figure 5. The ratio quickly exceeds 1 and stabilizes at 20 arcsec and stays approximately constant at 20 – 25% level then on larger scales converges back to unity.

This is compelling evidence that we are indeed observing central-satellite galaxy pairs sharing the most massive halos. This is also natural outcome of the luminosity segregation in that the most massive halos (hosting the brightest LBGs) are likely to have sub-structures massive enough to form satellite galaxies bright enough for us to detect. We have tried a similar neighborhood search for the  $U$ -band dropouts, but failed to detect the same trend. Because the  $U$ -band dropouts have larger area coverage thus larger number of bright sources, we have increased the magnitude cut for the brightest group up to  $R = 22.0$  but still the brightest group does not evidently have more neighbors than the rest. There are two possibilities that can explain this. First, due to the relatively shallow depth of our  $U$ -band data, we may be seeing only the bright end of the luminosity function which essentially has one-to-one correspondence between halos and galaxies. It is consistent with Adelberger et al. (2005)'s data that have comparable depth based on which he concluded that there is little evidence of galaxy multiplicity and that the fraction of dark halos hosting more than one galaxy is about 5%. A possibility is that the relatively poor seeing of our  $R$  band, which

is where galaxy detection is carried out, prevents detection and deblending of pairs that are closer than 2 arcsec.

## 6. The Halo Occupation Distribution at $z \sim 4$ and 5

So far we have discussed the measures of the angular correlation function of LBGs, the implied spatial correlation length, and we have reported evidence of a departure of the correlation function from a single power law. We have also shown direct evidence of sub-structure in the most massive halos in the form of number counts of faint LBGs around the brightest ones on scales  $\theta \leq 10$  arcsec. Finally, we have also measured clustering segregation, namely the fact that brighter LBGs are more strongly clustered in space. In order to understand these results in light of underlying physics, we need to compare with theoretical predictions through which quantitative interpretations of the result can be made.

Associating the spatial distribution of galaxies with that of dark halos requires an understanding of the relationship between galaxy properties and those of host halos, for example, galaxy colors, stellar mass or luminosity are correlated with circular velocity, total mass of halos and so forth. We do not yet know if all the halos above a certain mass threshold host galaxies with similar SEDs (colors) and luminosity to those of LBGs to be included in our sample. At  $z \sim 3$ , a population of red galaxies (heavily dust-enshrouded or old; DRGs), which are bright in the near IR have been found at similar redshifts with about half the space density of  $U$ -band dropouts ( $\mathcal{R} < 25.5$ ) (Franx et al. 2003; van Dokkum et al. 2003). Many of these galaxies would not have been selected via the Lyman Break technique. Moreover, the sub-mm galaxies, though their space density is much smaller ( $2.4 \pm 1.2 \times 10^{-6}$  Mpc $^{-3}$ ; Chapman et al. 2003), also coexist in the same redshift range. These high- $z$  populations (including LBGs) suffer from respective selection biases thus cannot be solely representative of high- $z$  population in general. The halo occupation distribution model provides us with a powerful tool that enables us to study the characteristics of different populations independently to study their relations to host halos. The HOD formalism have been successfully applied to various local galaxy samples (e.g. different luminosities, colors, spectral types etc.; Zehavi et al. 2004b).

We move on now to consider a simple model for the halo occupation distributions (HOD) function, which can be used to understand the phenomenology of the observed clustering properties of LBGs in physical terms, and derive its parameters. These include the minimum mass of halos that can host the observed galaxies and the average halo mass for each galaxy sub-sample. We will then use the best HOD parameters to discuss the inferred halo bias and its implications.

As discussed earlier, the angular correlation function can be considered to have two separate contributions, galaxy pairs from the same halo and two distinct halos.

$$w(\theta) = w_{1h}(\theta) + w_{2h}(\theta) \quad (6)$$

On large scales, only  $w_{2h}(\theta)$  contributes to the total angular correlation function because any galaxy pair with certain angular separation apart cannot come from the same halo. On the other hand, on small scales and on scales comparable to virial diameter of halos, both terms will be present with a ratio that depends on the degree of galaxy multiplicity. The two-halo term can be constrained from clustering measurements; however, the galaxy multiplicity function or halo occupation distribution (HOD) is not very well constrained at high- $z$  because of the still relatively small and shallow sample. Bullock et al. (2002) estimated the HOD from a sample of 800 LBGs with spectroscopic redshifts at  $z \sim 3$  based on a ground-based survey ( $\mathcal{R} < 25.5$ ; Steidel et al. 1998). Although this sample has the advantage of having spectroscopic information, the median luminosity of the sample is significantly brighter than our ACS sample at  $z \sim 4$ , and thus the number of faint members of pairs or multiplets is very likely quite small. Adelberger et al. (2005) estimate that at most 5% of their LBGs at  $z \sim 3$  (an extended version of the sample used by Bullock et al. 2002) are members of close pairs. We do not yet know the luminosity function of satellite LBGs; however, our neighborhood analysis discussed earlier for the  $B_{435}$ -band dropout sample at  $z \sim 4$  showed that a large fraction of excess number of neighbors comes from  $z_{850} > 26$  (galaxies counted as faint neighbors have  $25.2 < z_{850} < 27.0$ ). Using our template LBG spectrum,  $z_{850} = 26.0$  corresponds to  $\mathcal{R} = 25.5$  at  $z \sim 3$ , that is the limiting flux of Adelberger et al.'s sample. While the bright members of pairs and multiplets are certainly present in their sample, Adelberger et al.'s sample must be highly incomplete of satellite galaxies.

Once the halo power spectrum is given and an HOD model assigned, one can unambiguously determine the correlation function (Seljak 2000; Berlind & Weinberg 2002; Berlind et al. 2003) with suitable assumptions as to how galaxies distribute within halos (see later). We adopt a simple functional form motivated by semianalytical modelling (e.g. Wechsler et al. 2001). This model assumes that all galaxies are associated with dark matter halos and makes a simplifying assumption that the number of galaxies within a given halo depends only on the halo mass and can be modelled by a single power-law:

$$\begin{aligned} \langle N_g(M) \rangle &= (M/M_1)^\alpha && \text{if } M > M_{min} \\ &= 0 && \text{otherwise} \end{aligned} \quad (7)$$

where  $M_1$  is the typical halo mass at which there is on average one galaxy per halo,  $M_{min}$  is

the cutoff halo mass below which halos cannot host galaxies and  $\alpha$  is the power-law index, the efficiency of galaxy formation within halos of given mass  $M$ .

While these three parameters,  $M_1$ ,  $M_{min}$  and  $\alpha$  are sufficient to constrain the correlation function on large scales, the shape of the correlation function on small scales also depends on how galaxies populate within host dark halos. This is because the one-halo term  $w_{1h}$  is proportional to  $\langle N_g(N_g - 1) \rangle$  while  $w_{2h}$  is to  $\langle N_g \rangle$  (see Appendix A. for details). Berlind & Weinberg (2002) discussed what these effects are and their impact on the shape of the correlation function on small scales. This includes the scatter of  $N_g$  around the mean, galaxy concentration with respect to halo concentration, the existence of a central galaxy at all times and the galaxy velocity dispersion with respect to that of halos. These factors can be used to construct more sophisticated models to constrain the HOD once a larger galaxy sample becomes available. However, at high-redshift, the number of galaxies included in any sample (so far) remains much smaller than that in such surveys as 2dF or SDSS, hence a simple approach seems preferable. Therefore we make simplifying assumptions to this model as follows. We force the first galaxy to be placed at the center of host halos and the rest (satellite galaxies) largely follow the halo mass distribution for which we adopt an NFW profile (Navarro, Frenk & White 1997). The latter is consistent with the finding of Kravtsov et al. (2004) that the sub-halos in their simulations follow the distribution of dark matter within the halos.

In order to calculate  $w(\theta)$  we closely follow the recipe given by Hamana et al. (2004), the procedure of which is described in Appendix A. We generate a library of model  $w(\theta)$ 's for a wide range of  $(M_1, \alpha)$  and determine the best-fit  $w(\theta)$  that matches the abundance ( $n_g$ ) and the clustering strength ( $M_{min}$ ,  $\alpha$  and  $M_1$ ) simultaneously using  $\chi^2$  minimization. Note that  $M_{min}$  is not a free parameter once the space density is specified.

$$\begin{aligned} n_g(z) &= \int_{M_{min}}^{\infty} n_h(M) \langle N_g(M) \rangle dM \\ \langle n_g \rangle &= \frac{\int dz N(z) [dV(z)/dz] n_g(z)}{\int dz N(z) [dV(z)/dz]} \end{aligned} \quad (8)$$

where  $N(z)$  is the redshift selection function obtained from the simulations. Here we fix the observed number density to the incompleteness-corrected number density integrated down to  $z_{850} = 27.0$  for the fit. However, note that our results cannot be too sensitive to the exact value of  $\langle n_g \rangle$  because  $w(\theta)$  scales logarithmically with  $n_g$  (CHECK THIS).

Table 4 lists the HOD parameters obtained using this method for the  $B_{435}$  and  $V_{606}$ -band dropouts only. For the  $U$ -band dropouts, we are unable to put any robust constraints on

these parameters primarily because the HOD fit is most sensitive to  $w(\theta)$  at small separations. The  $w(\theta)$  measure of the  $U$ -band dropouts on such scales seems to indicate either fall-off or constant rather than steepening. This is more consistent with having the correlation function of two-halo term only, i.e. each observed galaxy belongs to a different halo, in which case  $w_{2h}$  stays relatively constant on small scales ( $\xi(r)$  actually falls off but the projection,  $w(\theta)$ , stays constant due to the contribution from projected galaxy pairs). Figure 6 shows the best-fit model  $w(\theta)$  for the full sample of  $B_{435}$  and  $V_{606}$ -band dropouts with the observational measures. Corresponding confidence levels for the HOD fits are illustrated in Figure 7.

The best-fit parameters are  $(M_{min}, \alpha, M_1) = (7 \times 10^{10} M_\odot, 0.7, 1.3 \times 10^{12} M_\odot)$  for the  $B_{435}$ -band dropouts and  $(5 \times 10^{10} M_\odot, 0.80, 1.0 \times 10^{12} M_\odot)$  for the  $V_{606}$ -band dropouts, respectively. Though selected with different filter systems and shallower, it is interesting to compare them to those of Hamana et al. (2004),  $(1.6 \times 10^{11} M_\odot, 0.5, 2.4 \times 10^{12} M_\odot)$ ,  $(1.4 \times 10^{11} M_\odot, 0.5, 1.4 \times 10^{12} M_\odot)$  for their LBGz4s and LBGz5s.  $M_{min}$  is found to be a factor of 2 – 3 smaller from our survey. This is hardly surprising because  $M_{min}$  depends mainly on the depth of given survey. Our sample is significantly deeper than theirs ( $\approx 1$  mag) and, because LBGs have compact morphology, more complete in the magnitude range in common. As a result, the overall clustering strength of our sample is weaker which is most directly reflected in  $M_{min}$ . The parameter  $M_1$ , the mass scale at which statistically there is one galaxy corresponding to each halo, is smaller in our case consistent with our expectations. On the other hand,  $\alpha$ , though it may be also dependent on  $M$  (thus the depth), this work and previous studies consistently show that it should be 0.5 – 1. Therefore within reasonable range of observable halo mass it can be approximated (to the zeroth order) as a constant, thus most independent of mass scale. Unfortunately, as can be seen in Figure 7, it is the least constrained one from the HOD fit. In principle, however,  $\alpha$  can be constrained independently via studies such as our neighborhood analysis or gravitational lensing surveys.

We also calculate  $\langle N_g \rangle_M$  (note the subscript “M” to distinguish the quantity from the previously mentioned  $\langle N_g \rangle$ ), the average number of galaxies per halo when integrated over a range of halo mass, the average number of galaxies per halo ( $= n_g/n_h$ ) and  $\langle M \rangle$  and the average mass of halos that host the observed LBGs (assuming the best-fit HOD parameters) as follows:

$$\begin{aligned} \langle N_g \rangle_M &= \frac{\int_{M_{min}}^{\infty} n_h(M) \langle N_g(M) \rangle dM}{\int_{M_{min}}^{\infty} n_h(M) dM} \\ \langle M \rangle &= \frac{\int_{M_{min}}^{\infty} M \langle N_g(M) \rangle n_h(M) dM}{\int_{M_{min}}^{\infty} \langle N_g(M) \rangle n_h(M) dM} \end{aligned} \quad (9)$$

For each sub-sample, we compute  $M_{min}$  that matches the number density, then  $\langle N_g \rangle_M$  and  $\langle M \rangle$  are computed using the best HOD parameters. Table 4 summarizes the results. Uncertainties are computed by propagating the bootstrap errors of  $w(\theta)$  after marginalizing  $M_1$  and  $\alpha$ . We find that a 30% and 20% of the halos harbor LBGs bright enough to be detected. This is a relatively high efficiency. Note that Adelberger et al. (2005) and Giavalisco & Dickinson (2001), based on the ground-based sample with  $\mathcal{R} \leq 25.5$ , argue that most halos at  $z \sim 3$  host a visible LBGs. While it is not clear if their claim is in quantitative discrepancy with our estimate, we note that possible evolutionary effects of from  $z \sim 4$  to  $z \sim 3$  remains unconstrained at this time. It is interesting, however, that the  $B_{435}$ -band dropouts with  $z_{850} \leq 26.0$  (B260), which have comparable absolute luminosity threshold to that of the  $U$ -band dropouts of  $\mathcal{R} \leq 25.5$  (U255), have  $\langle N_g \rangle_M \sim 0.5$ , similar to what Adelberger et al. (2005) have found (see their Figure 10). This suggests that LBGs at  $z \sim 3$  and 4 of similar luminosity also have similar duty-cycle. If the average galaxy luminosity is closely tied with halo mass, as suggested by the luminosity segregation, this suggests that one can simultaneously calibrate the galaxy formation recipe at different cosmic epochs using these constraints. Interestingly, when the same absolute magnitude cut is made to the  $V_{606}$ -band dropouts, we find that  $\langle N_g \rangle_M$  is a factor of 2 – 3 smaller. We postpone the interpretations to the next subsection. Finally, note that  $\langle N_g \rangle_M$  gets smaller for fainter LBGs because this is already built in the HOD formalism. Physically, there are two reasons why this might be the case. First, in low-mass halos, gas cooling is much more inefficient due to galactic wind or SNe feedback, thus as a result preventing galaxies to form. In addition, it is possible that the duty-cycle of galaxies may be mass-dependent such that lower-mass halos have shorter duty-cycle, thus resulting in a smaller value of  $\langle N_g \rangle_M$ .

We have also explored an alternative approach, which is to model central galaxies and satellites separately (e.g. Zheng et al. 2005, Kravtsov et al. 2004). In this model, the probability for a halo to have a central galaxy is a step function, namely either the halo has the galaxy or it does not have it, whereas the distribution of satellite galaxies follows a power-law.

$$\begin{aligned} \langle N_g(M) \rangle &= 1 + (M/M'_1)^{\alpha'} && \text{if } M > M'_{min} \\ &= 0 && \text{otherwise} \end{aligned} \tag{10}$$

We refer to this model as “one-plus” model as opposed to the previous one which we refer to as “pure power-law” model hereafter. Note that the normalization  $M'_1$  and the threshold mass  $M'_{min}$  have different physical meanings in this model compared to the previous one. In the present model the parameter  $M'_1$  is the halo mass at which there is one satellite galaxy (thus two galaxies in total) in the host halo. The parameter  $M'_{min}$  is conceptually the same

as  $M_{min}$  of the first model, except that now halos above this threshold value always have  $N_g \geq 1$ , while in the pure power-law model only a fraction of halos with  $M > M_1$  are host to more than one galaxy on average. Using the alternative model for the halo distribution function of Lyman-break galaxies we find that the best-fit parameters for the  $B_{435}$ -band dropouts are  $(M'_{min}, \alpha', M'_1) = (2 \times 10^{11} M_\odot, 1.3, 4 \times 10^{12} M_\odot)$ .

The  $\chi^2$  shows that the two HOD models appear to reproduce the observed  $w(\theta)$  equally well. In addition, they predict similar  $\langle N_g \rangle$  for relevant mass scales ( $10^{10} - 10^{13} M_\odot$ ). At the high-mass end ( $M > 10^{13} M_\odot$ ), however, the two models diverge from each other rather quickly. To constrain the HOD function in this mass range one needs a much larger sample covering significantly more area than the GOODS, because of the rarity of high-mass halos.

Finally, we observe that although the two models are equally good in reproducing the observations, this is very likely the result of the still relatively large uncertainties in the measure of  $w(\theta)$ . The rationale behind the “one-plus” model is that every single halo above  $M_{min}$  participates in forming observed galaxies. In contrast, “pure power-law” model allows a fraction of halos to form galaxies in some range of mass ( $M < M_1$ ). Whether this difference is a physical one or rather a selection effect is not known at high-redshift. However, we note that the built-in assumption of the “one-plus” model, that there is always one central galaxy (in our case, one LBG), in every halo above a mass threshold, naturally precludes the possibility of having other types of galaxies (i.e. non LBG) as the central galaxy. While such a limitation is not a problem in the local universe, it is very likely a misrepresentation of the situation in the high-redshift universe. For example, a number of observations have shown the existence of massive galaxies at  $z \sim 3$  whose UV spectral energy distribution is such that they would not be selected as Lyman-break galaxies. Such galaxies very likely have masses that are in the high-mass end of the LBG mass range (e.g. Shapley et al. 2004, van Dokkum et al. 2004). The “one-plus” model would not provide a fair representation of the HOD if such galaxies are relatively common at high redshifts. For these reasons we will limit the discussion only to the pure power-law HOD (“pure power-law”) model in what follows.

### 6.1. The Evolution of Halo Bias with Redshift

We compute the nonlinear autocorrelation function of matter  $\xi_m(\mathbf{r})$  at redshift  $z \sim 3, 4$  and  $5$  by adopting the algorithm by Peacock & Dodds (1996).  $\xi_m(\mathbf{r})$  is then inverted to  $w_m(\theta)$  using the Limber transform as follows:



$$w_m(\theta) = \frac{\int_0^\infty dz N^2(z) \int_{-\infty}^\infty [dx/R_H(z)] \xi_m([D_M(z)\theta]^2 + x^2)^{1/2}}{[\int dz N(z)]^2} \quad (11)$$

$D_M(z)$  is the proper motion distance and  $R_H(z)$  the Hubble radius at given redshift  $z$ . Using this method, average bias is calculated as a function of angular separations.

$$\langle b_{obs}(\theta) \rangle = \sqrt{\frac{w(\theta)}{w_m(\theta)}} \quad (12)$$

$\langle b_{obs}(\theta) \rangle$  monotonically decreases at small separations then stays constant at  $\theta \geq 70$  arcsec. We adopt  $\langle b_{obs}(100 \text{ arcsec}) \rangle$  as our linear bias value. Theoretical predictions of the galaxy and halo bias can be computed from the given halo model as follows:

$$\begin{aligned} \langle b_g \rangle &= \frac{1}{n_g} \int_{M_{min}}^\infty n_h(M) b_h(M) N_g(M) dM \\ \langle b_h \rangle &= \frac{1}{n_h} \int_{M_{min}}^\infty n_h(M) b_h(M) dM \end{aligned} \quad (13)$$

We use  $n_h(M)$  from the analytic halo model by Sheth & Tormen (1999, 2002) and the best-fit HOD parameters for  $N_g(M)$ . Note that halo bias  $\langle b_h \rangle$  is HOD-independent whereas  $\langle b_g \rangle$  is not. The observed galaxy number density is calculated by fitting the full sample to the Schechter luminosity function after correcting for photometric incompleteness (e.g. Giavalisco 2005) and integrating down to each magnitude cut (see Table 3). The error bars in the number density are derived by propagating the uncertainties from the Schechter LF fit.

Figure 8 shows the average galaxy bias from the clustering measures together with the predictions of  $\langle b_h \rangle$  and  $\langle b_g \rangle$  at  $z \sim 4$  and 5. Note that the abscissa represents the halo abundance ( $n_h$ ) for dashed lines and the galaxy abundance ( $n_g$ ) for solid lines and symbols ( $n_g = n_h$  if  $N_g \equiv 1$ ). The observed galaxy bias values are in good agreement with the CDM model predictions when the best-fit HOD parameters are assumed.

To compare the results from different cosmic epochs, it is important to remove the effect of the luminosity segregation which could be mistakenly interpreted as "evolution". We truncate each sample to the same absolute luminosity threshold to match that of our brightest sample, the  $U$ -band dropouts ( $R < 25.5$ ), the absolute magnitude of which is  $M_z < -20.0$ . This corresponds to  $R < 25.5$ ,  $z_{850} < 26.0$  and  $z_{850} < 26.6$  at  $z \sim 3, 4$  and 5,

respectively. Since these luminosity thresholds are similar to those of the U255, B260 and V265 sample, we compare the bias values for these magnitude cuts. Figure 9 illustrates how these bias values change with redshift compared to halo bias of various mass thresholds. Dashed lines indicate the evolution of average halo bias of constant halo mass threshold for  $M_{halo} = 10^{10}, 5 \times 10^{10}, 10^{11}, 5 \times 10^{11}, 10^{12}$  and  $5 \times 10^{12} M_{\odot}$  (from bottom) from Sheth & Tormen halo model. Lines serve as a guide to determine effective halo mass threshold of a given galaxy sample.

It is intriguing that our measures at  $z \sim 3$  and 4 imply that these galaxies are hosted by halos of mass  $5 \times 10^{11} M_{\odot} \lesssim M_{halo} \lesssim 10^{12} M_{\odot}$ , however, at  $z \sim 5$ , host halo mass is approximately  $10^{11} M_{\odot}$ , a factor of 4 – 5 times smaller than its lower- $z$  counterparts at the given fixed luminosity. Hamana et al. (2004) reported the average bias of their LBGz4s with similar absolute luminosity threshold,  $i' \leq 26.0$ , to be 3 – 4.5, consistent with our results. This implies that at higher- $z$ , the star-formation may have been more efficient hence galaxies of comparable luminosities were hosted in much lower-mass host halos. This result is, in fact, another manifestation of what we have mentioned in earlier subsection, that  $\langle N_g \rangle$  was a factor of 2 – 3 smaller than its lower- $z$  counterparts when the same absolute luminosity cut was made for a given choice of the HOD parameter set.

## 7. Summary

1. We have studied the spatial clustering properties of LBGs at three different cosmic epochs. We used three samples of LBGs which include two deep ACS-selected LBGs samples at  $z \sim 4$  and 5 down to magnitude limit of  $z_{850} \sim 27$  and the ground-based sample at  $z \sim 3$  down to  $R \sim 25.5$ . The ACS samples enable us to study the spatial distribution of the large-scale structure as well as of the small-scale whereas the ground-based sample allows us to probe the large-scale of bright LBGs selected from a large contiguous area.

2. We found that the clustering strength (the amplitude of  $w(\theta)$  or of  $r_0$ ) of LBGs at all redshifts that we have studied depends on the UV luminosity (rest-frame  $\lambda = 1700 \text{ \AA}$ ) of the galaxies. This luminosity segregation is in good quantitative agreement with previous investigations based on much brighter galaxy samples and we are able to extend this relationship robustly down to at least 1 mag fainter than previous studies. The faintest galaxy sub-sample has the spatial correlation length as small as  $2 h^{-1} \text{ Mpc}$ , only a half of that known for  $\mathcal{R} \leq 25.5$  sample. A physical implication is that galaxies brighter at UV wavelengths are hosted by more massive dark halos, implying that the star-formation is primarily regulated by local gravity and suggesting that other physical mechanisms (merging, interactions) are secondary drivers.

3. We have carried out neighborhood search around bright LBGs in our sample and counted the number of bright–faint galaxy pairs and discovered that the likelihood to find faint neighbor galaxies ( $z_{850} \geq m^*$ ) around bright ones ( $z_{850} \leq 24$ ) up to scales comparable to virial radius of dark halos, is at least 20 – 30 % higher than random LBG–LBG pair with a high significance. This behavior is commonly observed in high–resolution N–body simulations. For example, Kravtsov et al. (2004) measured the correlation function of halos above a given mass threshold (and thus of given number density) identified from such simulations at various cosmic epochs. They found that at  $z = 0$  the halo correlation function can be fairly well approximated by a power law at all probed scales. However, at higher redshifts, steepening occurs on small scales (progressively smaller scales with higher redshifts). As a result, power–law fits using the range of scales  $0.1 - 8 h^{-1}$  Mpc give systematically steeper value of  $\beta$  compared to the fits over the range  $\sim 0.3 - 8 h^{-1}$  Mpc. Figure 5 shows a similar behavior (in the angular domain) and it can be compared to Figure 12 of Kravtsov et al. (2004). The observed sub–structure is also consistent with the luminosity segregation in that brighter galaxies (more massive halos) are likely to have fainter galaxies (halo sub–structures). We do not yet know the relationship between the UV luminosity and the actual halo mass that they belong to. However, the clustering segregation gives weight to the interpretation that the most luminous LBGs hosted by the most massive halos tend to have satellite galaxies in halo sub–structures. Due to the relatively small dynamic range in magnitude of our survey, we are limited to the bright cut of  $z_{850} = 26.0$  and also to cumulative magnitude thresholds for our samples, however, future surveys that cover larger cosmic volume can complement our results from which we expect this effect to be more dramatic.

4. The measured correlation function indicates that at  $z \sim 4$  and 5, the steepening occurs on small scales thus the measure cannot be well described by a simple power–law. We also find that the scale at which the steepening occurs is comparable to the angular size of dark halos at given redshift range, hence we attribute this steepening feature to the distribution of galaxies within same halos. A simple HOD model with a suitable scaling law between halo mass and the number of galaxies seem to be able to explain both large–scale and small–scale behavior of the angular correlation function. We find the best parameters for LBGs at  $z \sim 4$  and 5 to be  $(M_{min}, \alpha, M_1) = (7 \times 10^{10} M_{\odot}, 0.7, 1.3^{12} M_{\odot})$  and  $(5 \times 10^{10} M_{\odot}, 0.8, 10^{12} M_{\odot})$ , respectively. With these parameters, we find that, on average, the number density of galaxies is by a factor of 4 – 5 short of that of dark halos for the full sample and that this discrepancy is smaller for bright galaxy samples. This suggests that duty–cycle of these populations may be shorter than the cosmic time span covered by the observations as suggested by shallower surveys, but at the same absolute luminosity cut, our results are in good agreement with shallower surveys. However, at  $z \sim 3$ , our measures do not indicate the similar steepening but is more consistent with constant or fall–off of the correlation

function. We interpret this discrepancy to be caused by difference in survey depth, that shallower surveys tend to pick up only bright LBGs located at the deepest potential well of dark matter halos and not satellites (which are usually fainter) within halo sub-structures that contribute significantly to create this small-scale feature.

5. The scaling law of the correlation length or galaxy bias as a function of volume density shows similar trend to that expected for dark halos implying that our measures fully support the biased galaxy formation scenario predicted by the cold dark matter framework. This suggests that LBGs flag the sites of dark halos efficiently, however, not every halo is lit up at the same time. This has to do with the fact that the duty-cycle of LBGs is shorter than the cosmic time spanned by the observations (0.3 – 0.5 Gyr), therefore only a fraction of halos are lit up by star-formation at any given time. In addition, a HOD that scales with halo mass, might be an indication that duty-cycle is also mass-dependent such that higher-mass halos may have longer duty-cycle than their lower-mass counterparts.

6. We truncate each sample to a fixed absolute luminosity and compute average bias of these galaxies. Galaxies are hosted by progressively higher mass halos with time that at  $z \sim 5$ , galaxies are hosted by halos of mass  $\sim 10^{11} M_\odot$  whereas at  $z \sim 3$ , a factor of 5 – 10 more massive. Given the same luminosity threshold, the implication is that at higher- $z$  the star-formation was more efficient.

We thank Cristiano Porciani for helpful assistance. K. L. acknowledges Takashi Hamana for kindly providing his halo code for model comparisons. We are also grateful to the entire GOODS team and particularly, Tomas Dahlen, who have put great efforts into calibrating many of the GOODS ground-based data sets, which made our ground-based measures possible.

### A. $w(\theta)$ and Halo Occupation Function

For a given set of  $(M_1, \alpha)$  with a fixed number density  $\bar{n}_g$ , the minimum mass  $M_{min}$  is determined by matching the number density of the observed galaxies  $\bar{n}_g$  with that expected from the halo model as follows:

$$n_g(z) = \int_{M_{min}}^{\infty} dM n_h(M) \langle N_g(M) \rangle \quad (A1)$$

$$\bar{n}_g = \frac{\int dz N(z) [dV/dz] n_g(z)}{\int dz N(z) [dV/dz]} \quad (A2)$$

where  $N(z)$  is the normalized redshift selection function and  $dV/dz$  is the comoving volume element per unit solid angle. The contribution from 1-halo and 2-halo components are computed from their respective galaxy power spectrum,  $P_g^{1h}(k, z)$  and  $P_g^{2h}(k, z)$ .  $w(\theta)$  is the inverse Fourier transform of the total power spectrum,  $P_g(k, z)$ :

$$w(\theta) = \int dz N(z)^2 \left(\frac{dr}{dz}\right)^{-1} \int dk \frac{k}{2\pi} P_g(k, z) J_0(r(z)\theta k) \quad (\text{A3})$$

where  $J_0$  is the Bessel function of the first kind.

The 1-halo contribution to the power spectrum is given as:

$$P_g^{1h}(k, z) = \frac{1}{n_g(z)^2} \int dM \frac{dn_h}{dM} \langle N_g(N_g - 1) \rangle |y(k, M)|^p \quad (\text{A4})$$

where  $y$  is the normalized Fourier transform of the halo mass profile (Seljak 2000; Scherrer & Bertschinger 1991). We further assume that each halo has an NFW profile with the concentration parameter varying with the halo mass as found by Bullock et al. (2001). The parameter  $p$  is taken to be  $p = 1$  if  $\langle N_g(N_g - 1) \rangle < 1$ , and  $p = 2$  otherwise (Seljak 2000).

The 2-halo term contribution to the galaxy power spectrum according to the linear halo bias model (Cole & Kaiser 1989; Mo & White 1996) is:

$$P_g^{2h}(k, z) = P_{lin}(k) \left\{ \frac{1}{n_g(z)} \int dM \frac{dn_h}{dM} \langle N_g(M) \rangle b(M) y(k, M) \right\}^2 \quad (\text{A5})$$

where  $P_{lin}(k)$  is the linear dark matter power spectrum and  $b(M)$  is the linear halo bias by the fitting function of Sheth & Tormen (1999).

## REFERENCES

- Adelberger, K. et al. 1998, ApJ, 505, 18
- Adelberger, K. & Steidel, C. 2000, ApJ, 544, 218
- Adelberger, K. et al. 2005, ApJ, 619, 697
- Benoist, C. et al. 1996, ApJ, 472, 452
- Berlind, A. A. & Weinberg, D. H. 2002, ApJ, 575, 587
- Berlind, A. A. et al. 2003, ApJ, 593, 1
- Bertin, E. & Arnouts, S. 1996, A&AS, 117, 393
- Bullock, J. et al. 2001, MNRAS, 321, 559
- Bullock, J. et al. 2002, MNRAS, 329, 246
- Chapman, S. et al. 2003, Nature, 422, 695
- Cole, S. & Kaiser, N. 1989, MNRAS, 237, 1127
- Daddi, E. et al. 2003, ApJ, 588, 50
- van Dokkum, P. et al. 2003, ApJ, 587, 83
- Ferguson, H. et al. 2004, ApJ, 600, L107
- Foucaud, S. et al. 2003 A&A, 409, 835
- Franx, M. et al. 2003, ApJ, 587, L70
- Giavalisco, M. et al. 1998, ApJ, 503, 543
- Giavalisco, M. 2002, ARA&A, 40, 579
- Giavalisco, M. & Dickinson, M. E. 2001, ApJ, 550, 177
- Giavalisco, M. et al. 2004a, ApJ, 600, L93
- Giavalisco, M. et al. 2004b, ApJ, 600, L103
- Giavalisco, M. 2005, *proceedings from Wide-Field Imaging from Space* eds. Tim McKay, Andy Fruchter, and Eric Linder

- Gunn, J. E. & Oke, J. B. 1975, *ApJ*, 195, 225
- Hamana, T. et al. 2004, *MNRAS*, 347, 813
- Kravtsov, A. et al. 2004, *ApJ*, 609, 35
- Landy, S. & Szalay, A. 1993, *ApJ*, 412, 64
- Ling, E. N., Barrow, J. D. & Frenk, C. S. 1986, *MNRAS*, 223, 21
- Madau, P. et al. 1995, *ApJ*, 441, 18
- Madau, P. et al. 1996, *MNRAS*, 283, 1388
- Miley, G. et al. 2004, *Nature*, 427, 47
- Mo, H. J., & White, S. D. M. 1996, *MNRAS*, 282, 347
- Navarro, J. F., Frenk, C. S. & White, S. D. M. 1997, *ApJ*, 462, 563
- Norberg, P. et al. 2001, *MNRAS*, 328, 64
- Ouchi, M. et al. 2004, *ApJ*, 611, 685
- Ouchi, M. et al. 2005a, *ApJ*, 620, L1
- Ouchi, M. et al. 2005b, submitted to *ApJ*
- Peacock, J. A. & Dodds, S. J. 1996, *MNRAS*, 280, 19
- Peebles, P. J. E. 1980, *The Large-Scale Structure of the Universe* (Princeton: Princeton Univ. Press)
- Porciani, C. & Giavalisco, M. 2002, *ApJ*, 565, 24
- Press, W. H. et al. 1992, *Numerical Recipes* (Cambridge: Cambridge Univ. Press)
- Riess, A. et al. 2004, *ApJ*, 600, L163
- Roche, N. & Eales, S. 1999, *MNRAS*, 307, 703
- Sheth, R. K. & Tormen, G. 1999, *MNRAS*, 308, 119
- Sheth, R. K. & Tormen, G. 2002, *MNRAS*, 329, 61
- Scherrer, R. J. & Bertschinger, E. 1991, *ApJ*, 381, 349

- Seljak, U. 2000, MNRAS, 318, 203
- Shapley, A. E. et al. 2004, ApJ, 612, 108
- Somerville, R. et al. 2004, ApJ, 600, L171
- Steidel, C. C. et al. 1995, AJ, 110, 2519
- Steidel, C. et al. 1998, ApJ, 492, 428
- Steidel, C. et al. 1999, ApJ, 519, 1
- Steidel, C. C. & Hamilton, D. 1993, ApJ, 105, 2017
- Steidel, C. C. et al. 2003, ApJ, 592, 728
- Vanzella, E. et al. 2005, A&A, 434, 53
- Wechsler, R. et al. 2001, ApJ, 554, 85
- White, S. D. M. & Reese, M. 1978, MNRAS, 183, 341
- Zehavi, I. et al. 2002, ApJ, 571, 172
- Zehavi, I. et al. 2004a, ApJ, 608, 16
- Zehavi, I. et al. 2004b, astro-ph/0408569
- Zheng, Z. et al. 2004, astro-ph/0408564



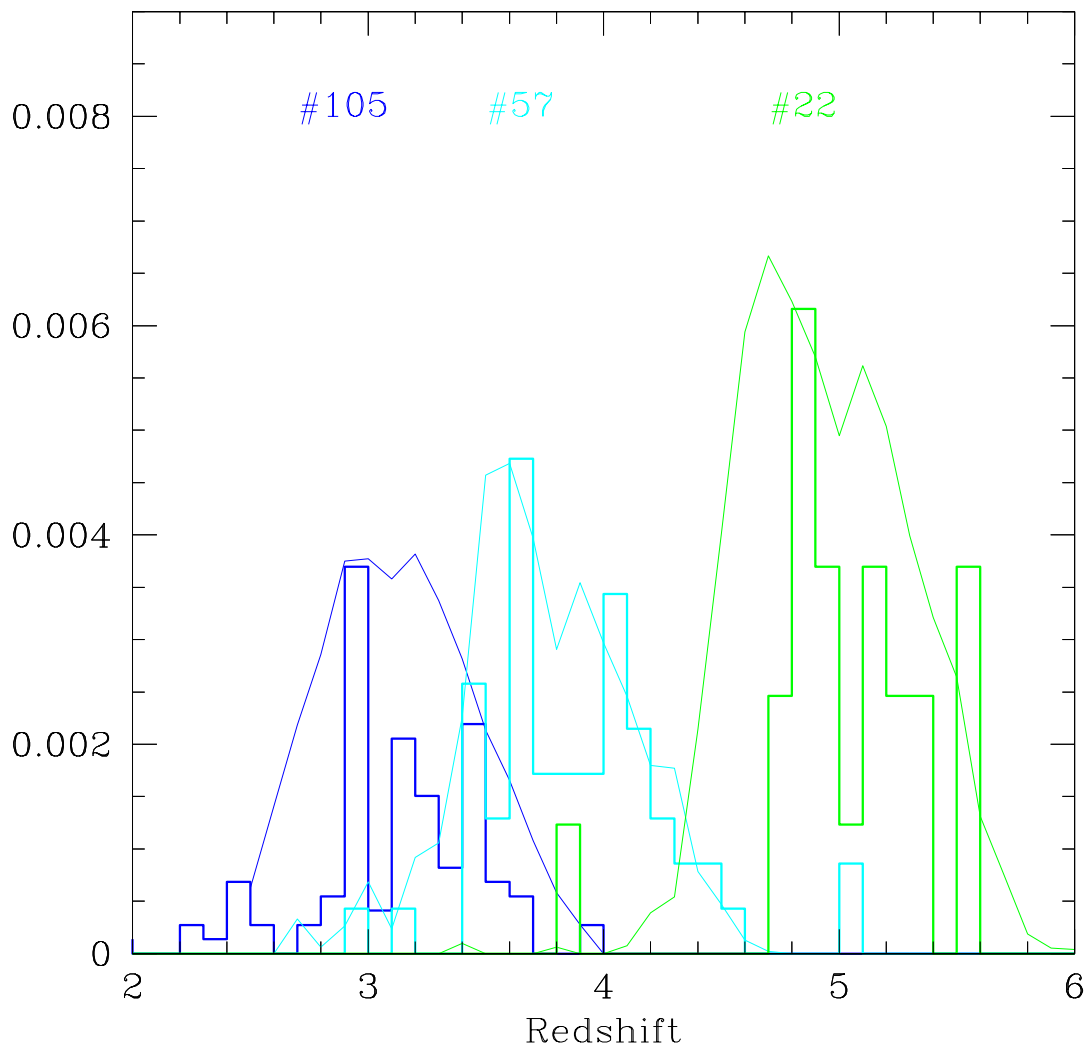


Fig. 1.— Redshift distribution functions  $N(z)$  of the  $U$ ,  $B_{435}$  and  $V_{606}$ -band dropouts (from left) estimated from Monte Carlo simulations. Coarser histograms indicate the distribution of spectroscopically confirmed objects to date whose numbers are specified on top of the plot. Histograms are arbitrarily normalized to match the distribution of the spectroscopic samples.

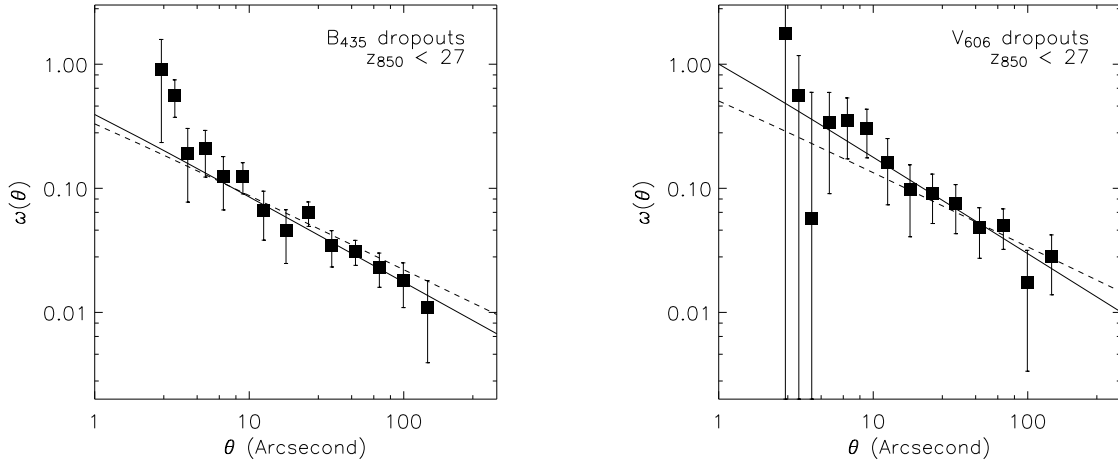


Fig. 2.— The angular correlation function  $w(\theta)$  of the  $B_{435}$  (left panel) and  $V_{606}$ -band dropouts (right panel). The points are the measure from the data corrected for the integral constraint ( $IC$ ) together with the best-fit power-laws. Solid line shows the results when the slope is allowed to vary and the dashed line shows the result when the slope is fixed to  $-0.6$ . The fit is done including angular separations  $\theta > 10$  arcsec only. While the data can be well described by a single power-law on large scales, a large departure from a power-law on scales  $\theta < 10$  arcsec is observed.

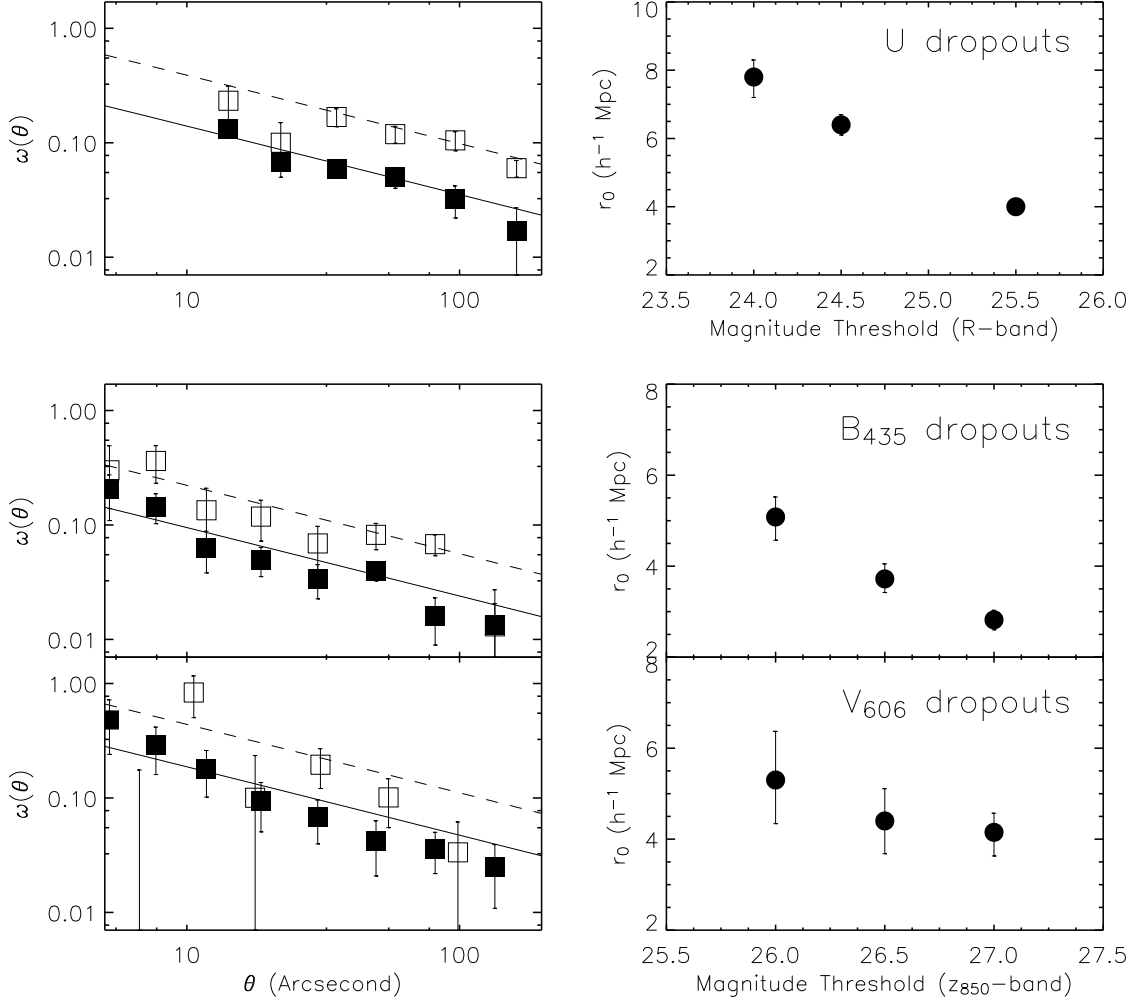


Fig. 3.— Left panels: The angular correlation function  $w(\theta)$  of the  $U$ ,  $B_{435}$ ,  $V_{606}$ -band dropouts (from top). Filled symbols show the measures from the full sample (the ACS-based:  $z_{850} < 27.0$ , the ground-based:  $R < 25.5$ ) while open symbols from the brightest sub-sample (the ACS:  $z_{850} < 26.0$ , the ground-based:  $R < 24.0$ ) together with the best-fit power-law when the slope is forced to be  $\beta = 0.6$ . The correlation amplitude,  $A_w$ , is increased by a factor of more than 2 for the brighter groups in each case. Right panels: The spatial correlation length  $r_0$  is shown as a function of magnitude thresholds made to define each sample. Note that top-right panel is  $R$ -based ( $R \leq 24.0, 24.5$  and  $25.5$ ), whereas the rest is  $z_{850}$ -based ( $z_{850} \leq 26.0, 26.5$  and  $27.0$ ).

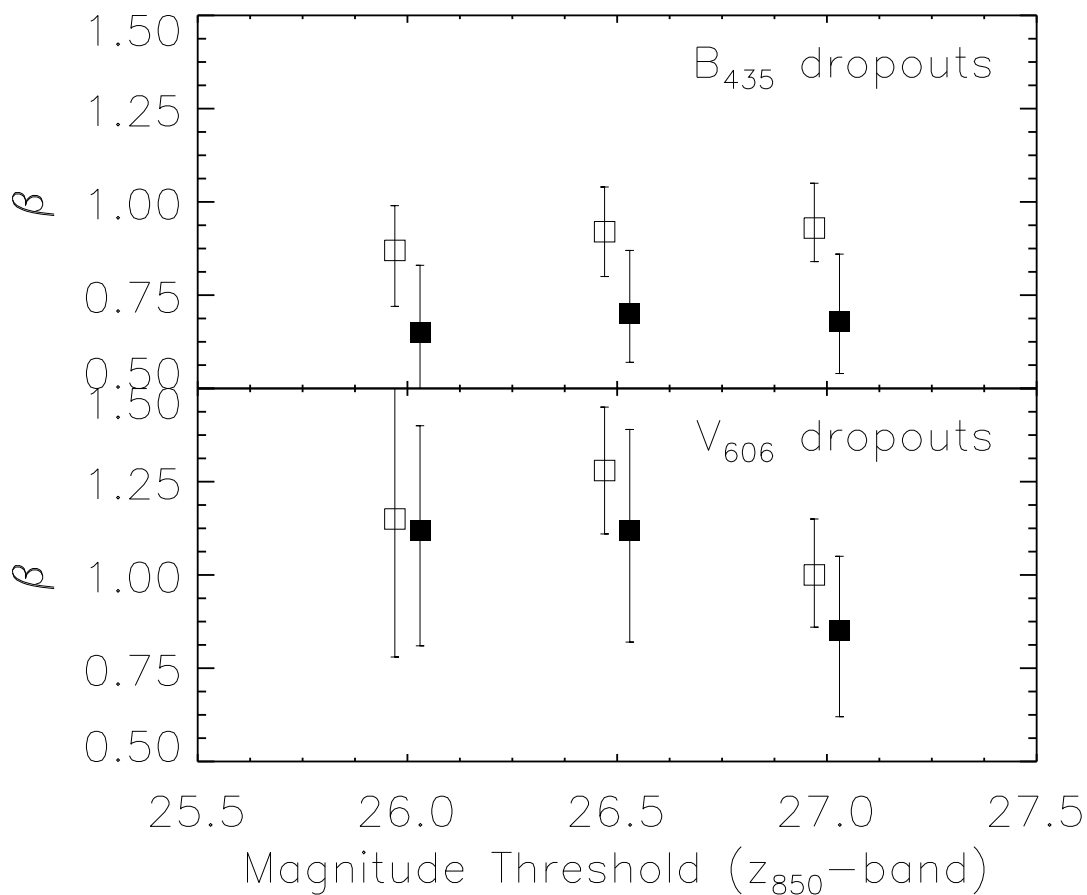


Fig. 4.— The steepening of the correlation slope on small scales: Both panels show the best-fit slope of the correlation function for samples with given apparent magnitude threshold. Filled (Open) symbols show the slope  $\beta$  when fitted to a single power-law without (with) the observational measures at angular separations of  $\theta < 10$  arcsec. This is due to an excess number of physically close galaxy-pairs causing a significant departure from a pure power-law at small separations.

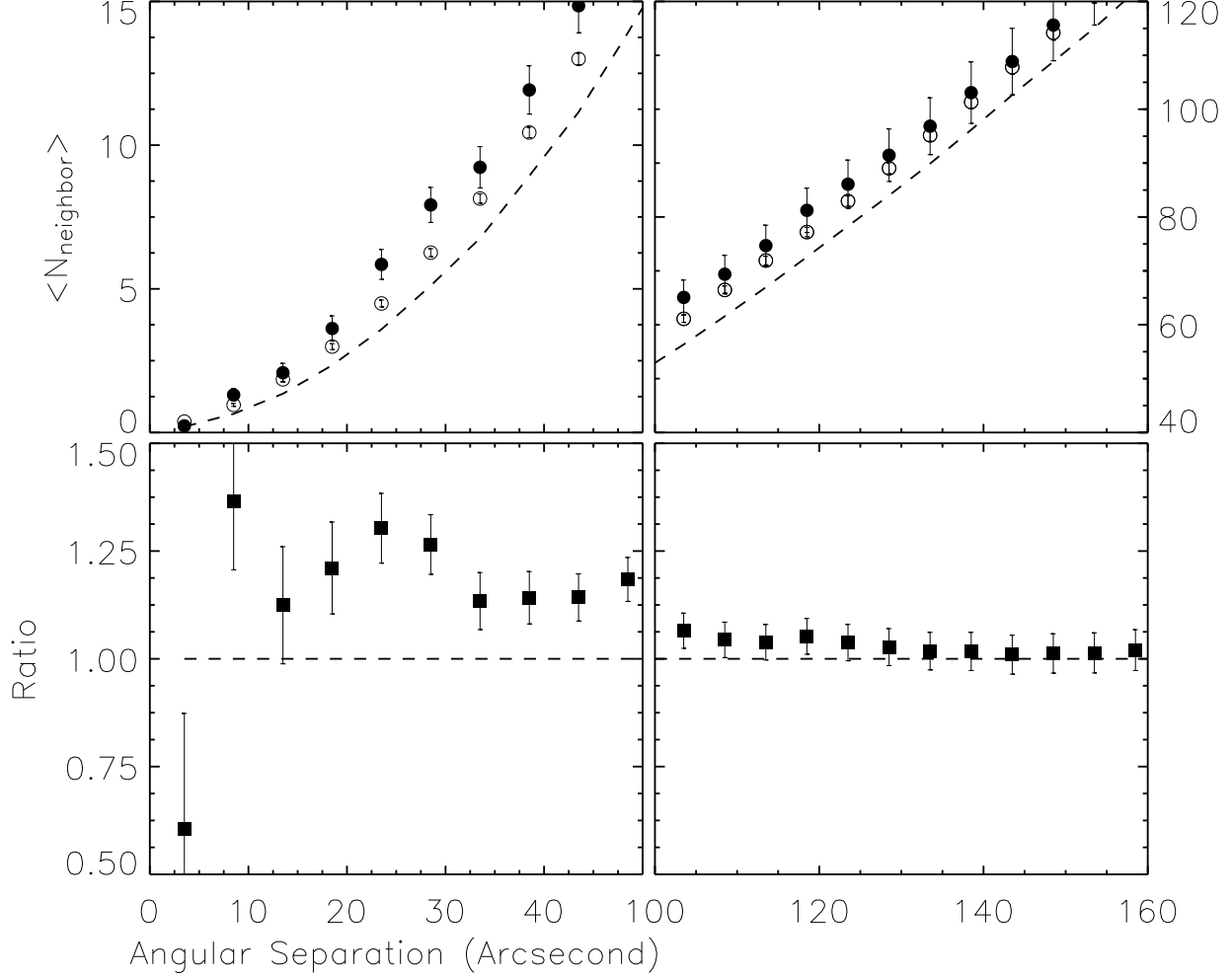


Fig. 5.— Top panels show the average number of faint LBG neighbors ( $z_{850} \geq m^*$ ) as a function of angular separation around two bright groups,  $z_{850} < 24.0$  (filled) and  $24.0 \leq z_{850} \leq m^*$  (open), together with what is expected for purely random distributions ( $w = 0$ ) shown as dashed lines. The error bars represent Poissonian errors. Bottom panels show the ratio of the two quantities shown in the top panels. Taking the ratio of the two essentially removes the effect from the projected galaxy pairs, providing a better indication of the true excess due to physical pairs. The galaxies that belong to the brightest group ( $z_{850} < 24.0$ ), on average, have more number of faint LBG neighbors ( $3\sigma$  significance) than the other group ( $24.0 \leq z_{850} \leq m^*$ ), most pronounced at  $0 < \theta < 30$  arcsec. The ratio stays constant up to  $\theta \sim 100$  arcsec (physical scale comparable to the correlation length) then slowly drops down to unity. This is consistent with halo sub-structure interpretation because when the angular separation is comparable to typical distance between near-by halos,  $\langle N_{\text{neighbor}} \rangle$  is dominated by clustering rather than halo sub-structure.

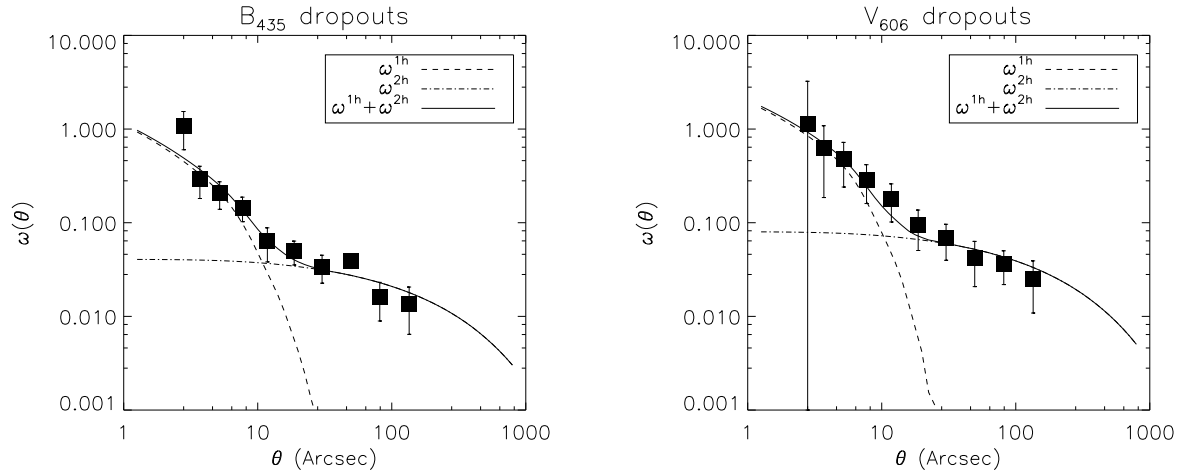


Fig. 6.— The two component fit with the best HOD parameters is shown together with the observed angular correlation function. The dashed line shows the 1-halo contribution and the dashed-dot line shows the 2-halo contribution to the final  $w(\theta)$ . The solid line is the sum of the two contributions. The best-fit HOD parameters are  $M_{min} = 7 \times 10^{10} M_{\odot}$ ,  $M_1 = 1.3 \times 10^{12} M_{\odot}$  and  $\alpha = 0.65$ . Right: the  $V_{606}$ -band dropouts: The best-fit HOD parameters are  $M_{min} = 5 \times 10^{10} M_{\odot}$ ,  $M_1 = 1.0 \times 10^{12} M_{\odot}$  and  $\alpha = 0.8$ .

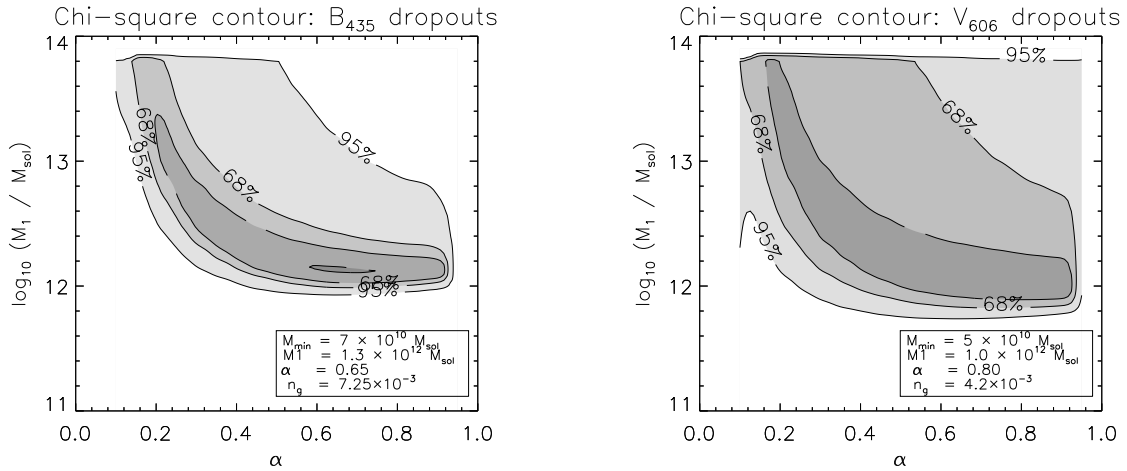


Fig. 7.— The  $\chi^2$  contour map of the HOD fits overlaid with confidence intervals for the  $B_{435}$  (left) and  $V_{606}$ -band (right) dropouts:  $M_1$  vs.  $\alpha$ . The contour lines show  $\Delta\chi^2 = 2.3$  and  $6.2$ , corresponding to 68% and 95% confidence levels. Boxes on the bottom right corners show the best-fit HOD parameter values and the number density.

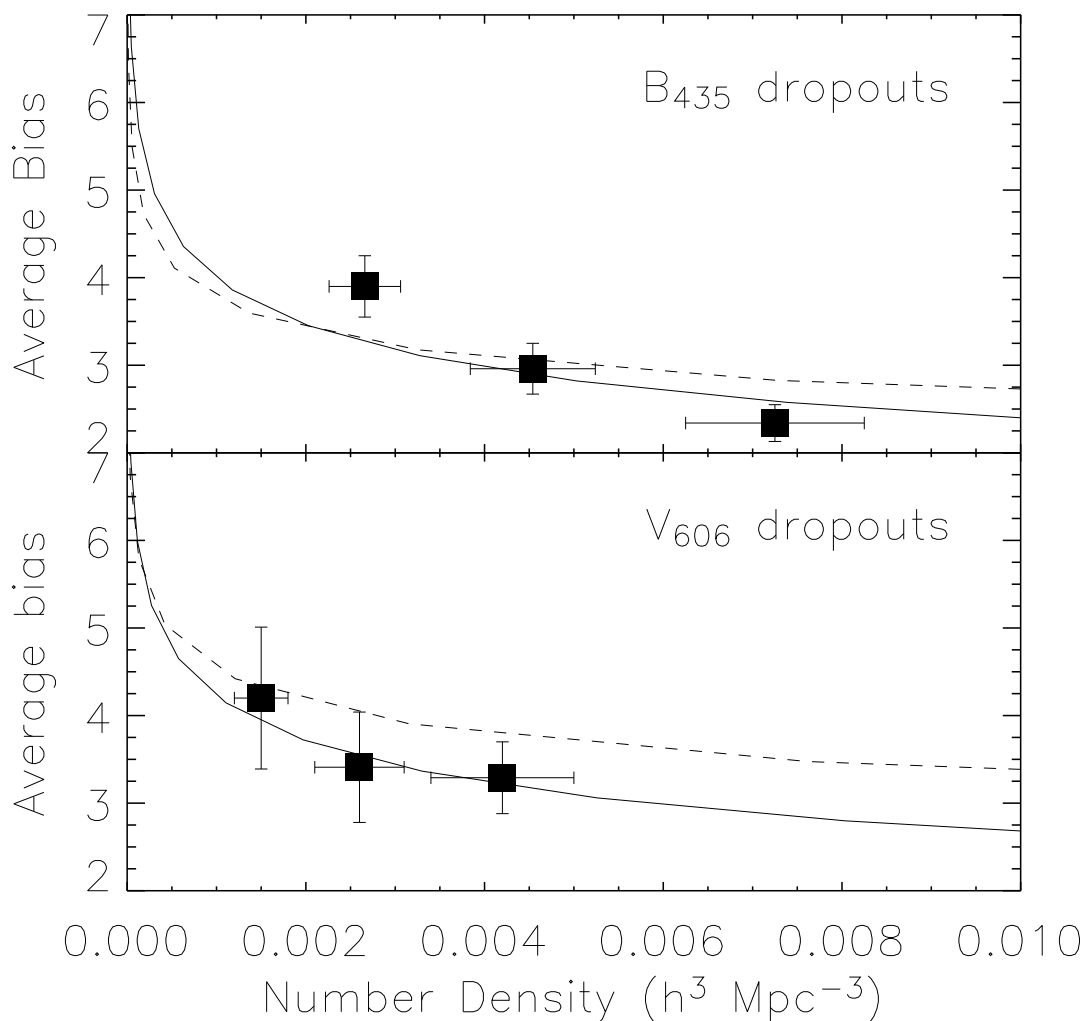


Fig. 8.— The average bias vs the galaxy (or halo) abundance: The data points and solid lines represent the average galaxy bias from the correlation measures and predictions as a function of galaxy number density, respectively. The average bias is computed as linear bias (Sheth & Tormen 2002) weighted by the best-fit HOD to account for the galaxy multiplicity. The dashed lines show the average halo bias as a function of halo number density. If there is one-to-one correspondence between halos and galaxies, then the two coincide.



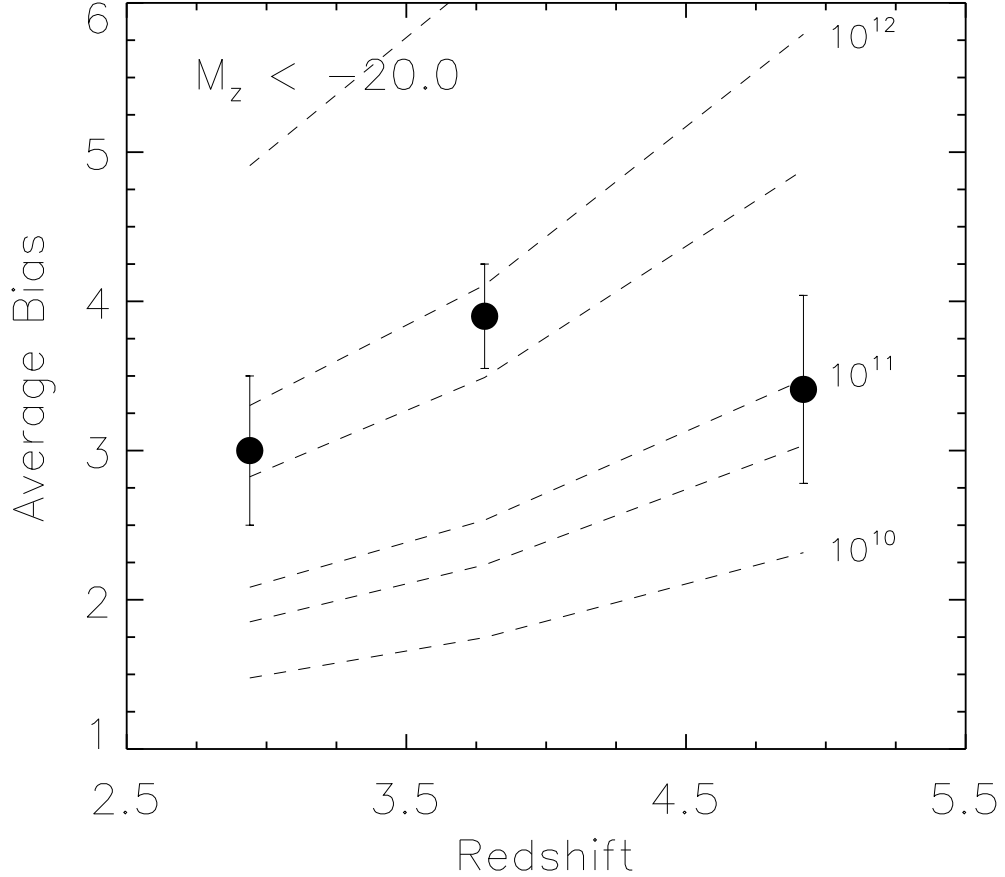


Fig. 9.— The evolution of the average bias as a function of redshift: the data points indicate the average bias implied for the  $U$ ,  $B_{435}$  and  $V_{606}$ -band dropouts at the fixed absolute luminosity threshold  $M_z < -20.0$ , this corresponds to  $\mathcal{R} \leq 25.5$  at  $z \sim 3$ . The dashed lines show the predicted linear bias from the Sheth & Tormen model for halo mass  $M_{halo} \geq M_{min} = 10^{10}, 5 \times 10^{10}, 10^{11}, 5 \times 10^{11}, 10^{12}$  and  $5 \times 10^{12} M_\odot$  (from bottom). At  $z \sim 3$  and 4, the observed galaxies are hosted by dark halos of similar mass ( $5 \times 10^{11} M_\odot - 10^{12} M_\odot$ ). At  $z \sim 5$ , the observed clustering strength of the galaxies implies that they are hosted by less massive halos,  $M_{halo} \sim 10^{11} M_\odot$ . This suggests that star-formation may have been more efficient at  $z \sim 5$ .

Table 1: The space-based dataset

Field	A <sup>a</sup>	$\sigma(B_{435})^b$	$\sigma(V_{606})^b$	$\sigma(i_{775})^b$	$\sigma(z_{850})^b$	$N_{LBG,4}^c$	$N_{LBG,5}^c$
GOODS-N	160.0	29.00	29.08	28.33	28.09	1169	502
GOODS-S	160.0	28.88	29.05	28.34	28.06	1294	376

<sup>a</sup>Survey area, in units of arcmin<sup>2</sup>

<sup>b</sup>1  $\sigma$  surface brightness fluctuations within 1 arcsec<sup>2</sup> apertures

<sup>c</sup>Number of  $B_{435}/V_{606}$ -band dropout Lyman break galaxies

Table 2: The ground-based dataset

Field	A	$\sigma(U)^a$	$\sigma(B)^a$	$\sigma(R)^a$	$N_U^b$
extended GOODS-S	600	29.42	29.75	28.95	1612

<sup>a</sup>1  $\sigma$  surface brightness fluctuations within 1 arcsec<sup>2</sup> apertures

<sup>b</sup>Number of  $U$ -band dropout Lyman break galaxies

Table 3: The LBG abundance, the angular correlation function and the inferred correlation lengths

Flavor	Sample	$n_g (\times 10^{-3})$	$A_{w,0}$	$\beta_0$	$r_{0,0}$	$A_{w,1}$	$\beta_1$	$r_{0,1}$
$U$	$R \leq 25.5$	$3.3 \pm 1.0$	$0.56^{+0.04}_{-0.04}$	0.6	$4.1^{+0.1}_{-0.2}$	$0.52^{+0.28}_{-0.20}$	$0.63^{+0.11}_{-0.12}$	$4.0^{+0.2}_{-0.2}$
$U$	$R \leq 24.5$	$0.7 \pm 0.3$	$1.16^{+0.06}_{-0.08}$	0.6	$6.5^{+0.2}_{-0.3}$	$0.54^{+0.23}_{-0.16}$	$0.44^{+0.08}_{-0.08}$	$6.4^{+0.3}_{-0.3}$
$U$	$R \leq 24.0$	$0.2 \pm 0.1$	$1.58^{+0.14}_{-0.17}$	0.6	$7.8^{+0.4}_{-0.5}$	$0.84^{+0.68}_{-0.32}$	$0.52^{+0.12}_{-0.11}$	$7.8^{+0.5}_{-0.6}$
$B_{435}$	$z_{850} \leq 27.0$	$7.3 \pm 1.0$	$0.38^{+0.04}_{-0.05}$	0.6	$2.9^{+0.2}_{-0.2}$	$0.42^{+0.32}_{-0.26}$	$0.69^{+0.16}_{-0.15}$	$2.8^{+0.2}_{-0.2}$
$B_{435}$	$z_{850} \leq 26.5$	$4.5 \pm 0.7$	$0.60^{+0.10}_{-0.06}$	0.6	$3.9^{+0.3}_{-0.3}$	$0.75^{+0.56}_{-0.37}$	$0.70^{+0.17}_{-0.13}$	$3.7^{+0.3}_{-0.3}$
$B_{435}$	$z_{850} \leq 26.0$	$2.7 \pm 0.4$	$0.99^{+0.14}_{-0.13}$	0.6	$5.3^{+0.4}_{-0.5}$	$0.64^{+0.98}_{-0.45}$	$0.64^{+0.19}_{-0.19}$	$5.1^{+0.4}_{-0.5}$
$V_{606}$	$z_{850} \leq 27.0$	$4.2 \pm 0.8$	$0.76^{+0.13}_{-0.15}$	0.6	$4.4^{+0.5}_{-0.5}$	$1.00^{+1.68}_{-0.75}$	$0.85^{+0.20}_{-0.23}$	$4.2^{+0.4}_{-0.5}$
$V_{606}$	$z_{850} \leq 26.5$	$2.6 \pm 0.5$	$1.12^{+0.34}_{-0.25}$	0.6	$5.8^{+1.1}_{-0.8}$	$2.08^{+8.80}_{-1.76}$	$1.10^{+0.30}_{-0.27}$	$4.4^{+0.7}_{-0.7}$
$V_{606}$	$z_{850} \leq 26.0$	$1.5 \pm 0.3$	$1.70^{+0.42}_{-0.37}$	0.6	$7.5^{+1.1}_{-1.0}$	$3.88^{+12.89}_{-3.46}$	$1.10^{+0.31}_{-0.29}$	$5.3^{+1.1}_{-1.0}$

Note. — Number density ( $n_g$ ) and comoving correlation length ( $r_0$ ) are in units of  $h^3 \text{ Mpc}^{-3}$  and  $h^{-1} \text{ Mpc}$ , respectively. Quantities with secondary subscript “0” are when the slope is fixed to a fiducial value  $\beta = 0.6$ , those with subscript “1” are when both  $\beta$  and  $A_w$  are allowed to vary.

Table 4: The best-fit HOD parameters, the average number of galaxies per halo and the average halo mass for different luminosity thresholds

Flavor	Sample	$M_1^{a,b}$	$\alpha^b$	$\langle N_g \rangle_M$	$\langle M \rangle^a$
$B_{435}$	$z_{850} \leq 27.0$	$1.3 \times 10^{12}$	0.65	$0.31 \pm 0.14$	$(4 \pm 1) \times 10^{11}$
$B_{435}$	$z_{850} \leq 26.5$	$1.3 \times 10^{12}$	0.65	$0.38 \pm 0.13$	$(6 \pm 1) \times 10^{11}$
$B_{435}$	$z_{850} \leq 26.0$	$1.3 \times 10^{12}$	0.65	$0.49 \pm 0.13$	$(8 \pm 2) \times 10^{11}$
$V_{606}$	$z_{850} \leq 27.0$	$1.0 \times 10^{12}$	0.80	$0.20 \pm 0.18$	$(2 \pm 1) \times 10^{11}$
$V_{606}$	$z_{850} \leq 26.5$	$1.0 \times 10^{12}$	0.80	$0.24 \pm 0.19$	$(3 \pm 1) \times 10^{11}$
$V_{606}$	$z_{850} \leq 26.0$	$1.0 \times 10^{12}$	0.80	$0.30 \pm 0.21$	$(4 \pm 2) \times 10^{11}$

<sup>a</sup>All masses are in units of  $M_\odot$ .

<sup>b</sup>Note that the same HOD parameters,  $M_1$  and  $\alpha$ , constrained from the full sample were used for all subsamples